THESIS FOR THE DEGREE OF DOCTOR OF PHILOSOPHY

Numerical simulation and analysis of multi-scale cavitating flows using a hybrid mixture-bubble model

EBRAHIM GHAHRAMANI

Department of Mechanics and Maritime Sciences
CHALMERS UNIVERSITY OF TECHNOLOGY
Göteborg, Sweden 2020

Numerical simulation and analysis of multi-scale cavitating flows using a hybrid mixture-bubble model

EBRAHIM GHAHRAMANI
ISBN: 978-91-7905-385-7

Series number: 4852
ISSN 0346-718X

Department of Mechanics and Maritime Sciences
Chalmers University of Technology
SE-412 96 Göteborg
Sweden
Telephone + 46 (0)31-772 1000

Printed by Chalmers Reproservice
Göteborg, Sweden 2020

Numerical simulation and analysis of multi-scale cavitating flows using a hybrid mixture-bubble model

EBRAHIM GHAHRAMANI, 2020
Department of Mechanics and Maritime Sciences, Chalmers University of Technology

Abstract

The aim of this research is to model and analyse multi-scale cavitating flows with a certain emphasis on small sub-grid vapour structures. Cavitating flows include vapour structures with different length scales, from micro-bubbles to large cavities. The correct estimation of small-scale cavities can be as important as that of large-scale structures, since cavitation inception as well as the resulting noise, erosion, pressure shocks and strong vibrations occur at small time and length scales. For numerical analysis, while popular homogeneous mixture models are practical options for simulation of large-scale flows, they are normally limited in representation of the small-scale cavities due to high computational expenses and inherent simplifications. In this study, a hybrid cavitation model is developed by coupling a homogeneous mixture model with a Lagrangian bubble model. In this model, large cavity structures are modelled using a mixture model, while small sub-grid structures are tracked as Lagrangian bubbles.

The coupling of the mixture and the bubble models is based on an improved algorithm which is compatible with the flow physics and the governing equations are revised to take into account the bubble effect on the continuum flow.

The Lagrangian bubble model is based on a four-way coupling approach in which various effective forces on bubble transport are taken into account and a new algorithm is introduced to model bubble-bubble collisions. Besides, the bubble dynamics is calculated based on the local pressure effect by introducing an improved form of the Rayleigh-Plesset equation. The other contributions include implementing a new submodel for prediction of bubble break-up as well as correcting the bubble wall boundary condition and revising the void handling scheme.

Apart from the model development, for validation of the solver, a set of experimental tests on cavitating flow around a surface-mounted bluff body are performed in this study. Then, a multi-scale test case is simulated using both the new hybrid model and the traditional mixture model. The comparison of the results with the experimental data shows considerable improvements in both predicting the large cavities as well as capturing the small-scale structures using the hybrid model. More accurate results (as compared to the traditional mixture model) can be achieved even with considerably lower mesh resolution. The results, among others, show that small-scale cavities not only are important at the inception and collapse steps, but also influence the development of large-scale structures.

Keywords: Cavitation, Hybrid model, Multiphase flow, Multi-scale, Lagrangian bubble model, Homogeneous mixture model, CFD, OpenFOAM.

To my beloved parents

ACKNOWLEDGEMENT

Firstly, I would like to express gratitude to my parents, Habib and Shahla, for their love, prayers, caring and incredible sacrifices and continuing support for educating and preparing me for my future. There are not enough words in the whole world for me to describe how much I am grateful for having the best parents. My appreciation likewise extends to my lovely sisters, Fatemeh and Narges, for their love, support and encouragement throughout my life.

This work would not have been possible without the guidance, the support and the help of several individuals who in one way or another contributed and extended their valuable assistance in the preparation and completion of this study. I want to thank all of them. First and foremost, my utmost gratitude goes to my supervisor Prof. Rickard Bensow, for all the valuable discussions that we had as well as his guidance, trust and willingness to support during this project. I greatly acknowledge the freedom to explore my ideas and his valuable recommendations for my professional development. Truly THANK YOU for everything. Likewise, I very much appreciate the interesting meetings with my co-supervisor Associate Prof. Henrik Ström and his valuable suggestions for the model development. The remarkable experience of our group in cavitation modelling was also very helpful in my thesis. Special thank goes to Dr. Abolfazl Asnaghi for his well-documented earlier research and sharing ideas in cavitation modelling.

It was a great chance to be a part of the CaFE project during the course of my PhD. I thank all the project members for the fruitful meetings and the amazing social activities. I would like to particularly acknowledge all the efforts by the project coordinator, Prof. Manolis Gavaises (City, University of London), who also had insightful hints for me in developing the solver. During this project, I had two exciting study visits. Thank you Dr. Magdalena Neuhauser (Andritz Hydro) for hosting me, it was an unforgettable time for me in Vevey. I am very happy and thankful for the collaboration with you, Sébastien Bourgeois (Andritz Hydro), Saad Jahangir (TU Delft) and Prof. Christian Poelma (TU Delft). I wish to extend my gratitude to Dr. Steffen Schmidt (TU Munich) for helpful discussions about the cavitation models and useful comments for the project, as well as his research group for hosting me during my study visit in Munich. I further highly appreciate the interesting discussions about the finite mass transfer models with Sören Schenke (TU Delft).

My PhD journey has almost come to an end, and I have to say that it's been a long but exciting journey doing my PhD in Chalmers. I wish I could thank all the great people I feel lucky and happy for having them as friends and colleagues. In particular, I highly appreciate our manager, Prof. Jonas Ringsberg for all his kind and invaluable efforts in providing a pleasant atmosphere in our division. Thank you Dr. Arash Eslamdoost for your kind support and willingness to help. I further

appreciate you, my friend, Mohammad Hossein Arabnejad; in the past five years we have shared the office, have been together in many conferences and trips, and have had interesting discussions on cavitation and OpenFOAM. Thank you Carlo, Mohsen, Muye, Hedy, Jennie, Timofey, Johannes, Ioli, Fabian and many more. Last but not the least, my special and great friends, Ehsan and Fariborz, I want you to know how much I value your friendship, support and help in the past few years.

This thesis was partly funded through the EU H2020 project CaFE, a Marie Skłodowska-Curie Action Innovative Training Network; a joint research training and doctoral programme, grant number 642536. It was also funded by Kongsberg Maritime Sweden AB through the University Technology Centre in Computational Hydrodynamics hosted at the Department of Mechanics and Maritime Sciences at Chalmers. The computations were performed on resources at Chalmers Centre for Computational Sciences and Engineering (C3SE) and at National Supercomputer Centre (NSC) provided by the Swedish National Infrastructure for Computing (SNIC). In addition, part of the computations was performed using the resources provided by Leibniz Rechenzentrum (LRZ) at TU Munich.

Ebrahim Ghahramani,
Gothenburg, November 2020

LIST OF PAPERS

This thesis consists of an extended summary and the following appended papers. Papers I-IV are published and paper V is under review for journal publication.

Paper I E. Ghahramani, M. H. Arabnejad, and R.E. Bensow. Realizability improvements to a hybrid mixture-bubble model for simulation of cavitating flows. *Computers and Fluids*, 174:135-143, 2018.

Paper II E. Ghahramani, M. H. Arabnejad, and R.E. Bensow. A comparative study between numerical methods in simulation of cavitating bubbles. *International Journal of Multiphase Flow*, 111:339-359, 2019.

Paper III E. Ghahramani and R.E. Bensow. Analysis of the Finite Mass Transfer Models in the Numerical Simulation of Bubbly Flows. In *Proceedings of the 10th International Symposium on Cavitation*, p. 89-93, 2018.

Paper IV E. Ghahramani, S. Jahangir, M. Neuhauser, S. Bourgeois, C.Poelma, and R.E. Bensow. Experimental and numerical study of cavitating flow around a surface mounted semi-circular cylinder. *International Journal of Multiphase Flow*, 124:103191, 2020.

Paper V E. Ghahramani, H. Ström, and R.E. Bensow. Numerical simulation and analysis of multi-scale cavitating flows (submitted to Journal of Fluid Mechanics).

OTHER RELEVANT PUBLICATIONS

In addition to the appended papers, I have authored or co-authored the following publications/reports during my PhD:

Paper A S. Jahangir, E. Ghahramani, M. Neuhauser, S. Bourgeois, R. E. Bensow, C. Poelma. Experimental investigation of cavitation-induced erosion around a surface-mounted bluff body, (submitted to Wear).

Paper B E. Ghahramani and R.E. Bensow. Numerical prediction of small scale cavities using a coupled mixture-bubble model. *10th International Conference on Multiphase Flow*, Brazil, 19-24 May, 2019.

Paper C S. Jahangir, E. Ghahramani, M. Neuhauser, S. Bourgeois, R. E. Bensow, and C. Poelma. Experimental study of cavitation erosion around a surface-mounted semi-circular cylinder. *10th International Conference on Multiphase Flow*, Brazil, 19-24 May, 2019.

Paper D E. Ghahramani, and R.E. Bensow. Simulation of small-scale cavity structures through coupling of the mixture model with the discrete bubble model. In *Proceedings of the 20th Numerical Towing Tank Symposium (NuTTS 2017)*. p. 68-73, 2017.

Paper E E. Ghahramani, M. H. Arabnejad, and R.E. Bensow. A hybrid model for simulation of cavitating flows. *12th OpenFOAM® Workshop*, Exeter, UK, 24-27 July, 2017.

Paper F E. Ghahramani, and R.E. Bensow. A multi-scale Eulerian-Lagrangian model for simulation of cavitating flows. In *Proceedings of the 19th Numerical Towing Tank Symposium (NuTTS 2016)*. p. 37-42, 2016.

Report E. Ghahramani. Improvement of the VOF-LPT Solver for Bubbles. In *Proceedings of CFD with OpenSource Software, Edited by Nilsson. H., http://www.tfd.chalmers.se/ ∼ hani/kurser/OS_CFD_*2016, 2016.

CONTENTS

Nomenclature

α	Liquid volume fraction in the Eulerian framework
α_{Nuc}	Volume fraction of bubble nuclei
β	Liquid volume fraction in the Lagrangian framework
$\ddot{}$	Second temporal derivative
Δp	Pressure drop over the test section
$\dot{m}$	Rate of mass transfer between phases
$\dot{m}_c$	Rate of mass transfer during condensation
$\dot{m}_v$	Rate of mass transfer during vaporization
$\dot{}$	Temporal derivative
ε	Restitution coefficient during bubble collision
γ	Gas polytropic constant
$\mathbf{F}_a$	Bubble added mass force
$\mathbf{F}_b$	Bubble buoyancy force
$\mathbf{F}_d$	Bubble drag force
$\mathbf{F}_g$	Bubble gravitational force
$\mathbf{F}_l$	Bubble lift force
$\mathbf{F}_p$	Bubble pressure gradient force

$\mathbf{u}_b$ Bubble velocity vector

$\mathbf{x}_b$ Bubble position vector

μ_l Liquid dynamic viscosity

μ_m Mixture dynamic viscosity

μ_v Vapour dynamic viscosity

$\overline{\left(u_i' u_i'\right)_d}$ Mean square velocity difference over a distance equal to bubble diameter

ρ_b Bubble density

ρ_l Liquid density

ρ_m Mixture density

ρ_v Vapour density

σ Surface tension coefficient

σ_d Downstream cavitation number

τ_{ij} Viscous stress tensor

C_c Condensation rate coefficient

C_D Drag force coefficient

C_l Lift force coefficient

C_v Vaporization rate coefficient

d_b Bubble diameter

d_p Diameter of parent bubble

d_s Diameter of daughter bubble

D_{eq} Equivalent diameter of two bubbles

f_{bv} Break-up volume fraction

m_b Bubble mass

N_b Number of bubble parcels in a cell

n_i Number of bubbles represented by parcel i

N_{cell} Number of cells occupied by a parcel

N_{EL} Threshold number of cells for Eulerian to Lagrangian transition

N_{LE} Threshold number of cells for Lagrangian to Eulerian transition

p_1 Upstream pressure of the cavitation test section

p_2 Downstream pressure of the cavitation test section

p_∞ Far-field pressure

p_B Bubble pressure

p_v Vapour pressure

p_{2R} Surface-average pressure of the mixture over a concentric sphere with radius 2R

P_{coal} Coalescence probability

p_{g0} Initial equilibrium gas pressure

$p_{threshold}$ Threshold pressure of mass transfer (saturation pressure)

Q Volume flow rate in the test section

q_j Number of parcels in cell j

R Bubble radius

R_0 Initial equilibrium bubble radius

R_B Generic radius of bubble nuclei

$R_{eqv,i}$ Equivalent radius of a bubble group represented by parcel i

Re Reynolds number

t_d Drainage time of the liquid film between two bubbles

t_i Interaction time between two bubbles

u_{in}^+ Relative normal velocity of bubble i after collision

u_{in}^- Relative normal velocity of bubble i before collision

u_{th} Area-averaged velocity at the throat of the converging-diverging nozzle

V_i Volume of bubble i

$V_{cell,j}$ Volume of cell j

$v_{i,j}$ The void fraction of parcel i in cell j

V_{rel} Relative velocity between two bubbles

$V_{tot,i}$ Total volume of a bubble group represented by parcel i

We Weber number

1

Introduction

1.1 CAVITATION

Cavitation is the formation of vapour in a liquid when local static pressure of liquid falls below a critical pressure threshold. Without considering the effects of shear forces in flowfield, the pressure threshold is equal to the saturation pressure. The difference between cavitation and boiling is that cavitation occurs due to pressure drop while boiling is caused due to an increase in temperature. The very extensive and growing application field as well as its sophisticated physics have made cavitation a remarkable multidisciplinary topic in engineering.

For decades cavitation has been the subject of numerous studies with the aim to reduce its undesirable consequences in different industrial applications. Erosion, noise, vibration, load variation, blockage and efficiency loss in hydraulic machineries such as pumps, propellers and diesel injectors are some examples in this regard [1]. Recent advances in biomedical engineering, on the other hand, have caused significant interests in applying desirable consequences of cavitation. A non-exhaustive list of biomedical applications includes cancer cell histotripsy [2], drug and DNA delivery [3], kidney stone lithotripsy [4], Blood-Brain Barrier (BBB) opening and even to providing contrast with application in medical imaging [5]. Some of the other desirable instances are ultrasonic cleaning and mixing two or more dissimilar fluids such as in marine diesel engines. However, control of this phenomenon is still a challenge and a theoretical understanding is usually unachievable without significant simplifications. A main reason is that cavitating flows contain various structures with extensive ranges of length and time scales. For instance, the duration of the final stage of bubble or cavitating vortex collapse is of the order of one microsecond [1] while the erosion process might take place over the lifetime of a propeller. Also, the normal velocity of the interface can vary from a few meters per second to hundreds of meters per second, while the peak pressures can reach up to several thousands of bars for a few microseconds during

the last stages of cavity collapse. Therefore, there is an endless list of presented theoretical, experimental and numerical approaches to analyze this phenomenon.

1.2 NUMERICAL SIMULATION

Thanks to recent improvements in numerical models, today Computational Fluid Dynamics (CFD) is a reliable method to gain a more comprehensive and detailed understanding of the hydrodynamics of cavitation. CFD simulation can be a supplement or alternative to experimental measurements, which can be very expensive, suffer from scale effects, and give limited information; the latter is a particular problem in cavitating flows where the application of optical measurement techniques is often not possible. Nevertheless, due to the above-mentioned challenges, there is no unique CFD approach today that has sufficient performance for all cavitation problems. One of the most common sources of numerical challenges is the extensive range of temporal and spatial scales. Besides that, the vapour structures can have different multiphase topologies in cavitation. As an example, Figure 1.1 shows two types of cavity topologies with different length scales on the suction side of a hydrofoil. The image is extracted from the study by Foeth and van Terwisga [6] on the Twist11 hydrofoil. In this typical flow, on the leading edge a sheet cavity is well-developed, while further downstream we see an earlier shed cavity that is collapsing. While the sheet cavity is a large mixture of liquid and vapour, which can be considered as a single continuous pseudo-fluid separated from the main liquid by the interface, the downstream cavity is in fact a cloud of sparse bubbles and very small mixture cavities which are dispersed in the liquid. A common issue in cavitation CFD is to find a suitable method to simultaneously resolve (separated) large mixture regions and capture (disperse) small-scale vapour structures. It is important to note that the correct prediction and analysis of small-scale cavities can be as important as of large-scale structures, since cavitation initiates from micro nuclei and usually the resulting noise, erosion, pressure shocks and strong vibrations occur at the last stages of cavity collapse at the small time and length scales.

1.2.1 Eulerian mixture models

Most of the commonly used CFD models in engineering applications can be considered as homogeneous mixture models, in which the mixture of constituent phases is assumed to be a single fluid with no resolved liquid-vapour interface in each cell. Therefore, in each cell the two phases have the same velocity, pressure and temperature. Most often the cavitation/condensation is based on the flow pressure and other parameters such as dissolved gas pressure, surface tension and viscous forces are neglected in these models. Earlier studies have shown sufficient estimation of the shape of large vapour structures for different cavitating flows such as sheet cavity on hydrofoil (e.g. [7]), over convergent–divergent wedge

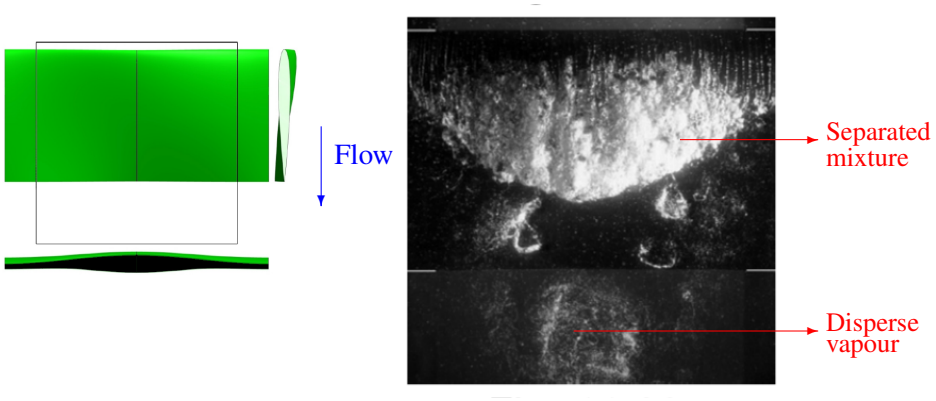

(a) (b)

Figure 1.1: (a) Top, side, and front view of the Twist 11 hydrofoil. The black outline indicates the viewing area. (b) Different cavity topologies and length scales over the hydrofoil (top-view)

(e.g. [8]) and fully cylindrical bluff bodies (e.g. [9]). However, the captured liquid–vapour interface is rather diffuse in these models and high grid resolutions with very small time steps are needed for adequate prediction of a sharp interface or capturing small structures. As the governing equations of the these models are solved in the Eulerian framework (similar to the continuity and momentum equations), in this report they are called Eulerian models, alternatively.

The most commonly used Eulerian mixture approaches can broadly be divided into two groups: equilibrium models and transport equation models (TEM). In equilibrium models, the two-phase cavitation regime is considered to be in mechanical and thermodynamic equilibrium. In these models, different phases and the interface are usually recognised based on the density value at each point and there are different approaches to find the pressure-density relation. For instance, Schnerr at al. [10] and Koop [11] used an equation of state (EoS) to find the pressure. Some other examples can be found in [12, 13, 14]. Once the EoS is defined, these models do not usually have empirical constants that need calibration for different problems; however to correctly capture pressure wave propagation, very small time steps are normally needed in the simulation. Therefore, these models are computationally expensive and they are usually applied to cavitating flows in small-scale geometries such as diesel injector nozzle flows.

Also in TEM, the multiphase flow is treated as a homogenous mixture and one set of continuity and momentum equations are used to calculate the mixture flow. In addition, a transport equation is solved for the vapour volume/mass fraction. For large-scale problems, such as cavitating ship propellers and turbines, it is more common to use incompressible transport equation models as they are less computationally expensive and can give rather satisfactory results using larger time steps, as compared to equilibrium models. The mass transfer rate is usually adjusted through a finite mass transfer source term in the transport equation which

is based on the difference between flow pressure and saturated vapour pressure. The most common mass transfer models in literature (e.g. [15]) can be interpreted as a simplified form of the Rayleigh-Plesset equation in which the dissolved gas pressure, surface tension and viscosity effects as well as the bubble inertia, are neglected. To improve the accuracy, however, some empirical constants are implemented in these models which should be tuned for each different simulation to adjust the mass transfer rate. Nevertheless, due to the simplifications in the estimation of mass transfer rate as well as the grid resolution dependency, in the common mixture models, cavity structures smaller than the grid size, such as small collapsing cavities, nuclei and bubbles or sparse clouds of bubbles (Figure 1.1), are not well represented. Correct estimation of small bubbles/nuclei are crucial in accurate prediction of cavitation inception, for instance. In the modelling of bluff body cavitation by Gnanaskandan and Mahesh [9], the numerical inception point is upstream of the separation point, since cavitation is assumed to occur as soon as the pressure drops below the vapour pressure. However, in corresponding experiments (e.g. [16]), cavitation does not occur immediately at the location where the pressure drops below the vapour pressure, but occurs downstream of the separation point. As an example for the the limitations of the Eulerian models in resolving the collapsing cavities, Asnaghi et al. [17] observed that the rate of phase change from vapour to liquid is over predicted for a shedding cloud on a hydrofoil which leads to an earlier collapse of the cloud in numerical modelling.

Therefore, it can be stated that while homogeneous mixture models are suitable options for representing large mixture regions, cavity structures smaller than the grid size, such as cavitation nuclei and bubbles, or sparse clouds of bubbles, are not well treated using these approaches. This is due to the simplifications in modelling phase change rate as well as the spatial and temporal resolution dependencies. Accurate simulation of sub-grid structures and their violent collapses and fast rebounds are very crucial in proper prediction of cavitation consequences.

1.2.2 Lagrangian bubble models

Apart from the widely used homogeneous mixture models, we have Lagrangian bubble models which can address some of the above-mentioned limitations. Here, the continuous liquid properties is calculated using Eulerian conservation equations whereas the vapor part is governed by the Newtonian motion of individual spherical bubbles or parcels of bubbles in the Lagrangian framework. The Lagrangian bubble models allow the consideration of a large number of effects that are deemed important for high-fidelity predictions of the smallest scales in cavitation phenomena, such as the effects of dissolved gas, liquid surface tension and viscous tension and accounting for bubble-bubble and bubble-wall interactions and turbulence effects on bubble motion and breakup. Lagrangian models can also give a more realistic estimation of cavitation dynamics especially for small-scale structures. In fact, cavitation inception studies are often performed using the Lagrangian approach. Besides that, using different bubble number/size spectra for

the liquid provides access to liquid (e.g. water) quality effects which is considered another major advantage.

These models have been extensively used in literature for simulation of cluster of bubbles, especially with dilute suspension. For example, Fuster and Colonius [18] proposed a Lagrangian formulation for bubbly flows based on the volume-averaged approach in which the continuum phase is solved from the averaged equations for the mixture (similar to the homogeneous mixture models) while the influence of the disperse phase is treated as source terms in the continuity, momentum, and energy equations. Small-scale cavitation (e.g. in medical treatments) is another field of application for this group in which the cavity length scale is around 1μm $\sim$ 1 mm and the interaction between pressure waves and bubbles are of great importance (e.g. [4]). Furthermore, there are a few studies in literature that apply Lagrangian modelling in real-case industrial problems at larger scales (see e.g. [19] and [20]). However, the Lagrangian models can be computationally expensive when the number of bubbles is large. Besides that, Lagrangian models are limited in representation of large and non-spherical vapour pockets which are not well-represented by the solution of the Rayleigh–Plesset equation. As explained earlier, for such structures an Eulerian mixture model is a more suitable option. Therefore, considering the cavity categorization based on the length scale (depicted in Figure 1.1), we see that for a group of cavities Eulerian mixture models are more suitable and Lagrangian bubble models suffer from theoretical/computational limitations, while the reverse case applies for the other cavity group, and finding an appropriate model that efficiently resolves both topologies is an issue.

1.2.3 Hybrid models

A solution to this problem can be a hybrid model in which large cavity structures are resolved using an Eulerian mixture model, while small sub-grid structures as well as sparse bubble clusters are tracked as Lagrangian bubbles. Hybrid Eulerian-Lagrangian solvers have gained more popularity in recent years for simulation of multi-scale applications such as atomizing gas-liquid flows (e.g. [21], [22], [23] and [24]). As similar approaches have been applied in cavitation modelling, it is necessary to consider some important distinctions between cavitation and atomization applications. In the mentioned hybrid models for atomizing flows (except [24]), it has been assumed that the Lagrangian particles do not occupy any volume in the Eulerian description which is valid when the Lagrangian formulation is used only in dilute regions of a flow. Also, the resulting model will be useful in situations where continuous phase density is very low in comparison to the dispersed phase density [24], such as liquid spray applications. However, in cavitating flows we encounter the opposite case since the continuous phase density (water) is much larger than the (vapour) bubble density and such an assumption is not valid. Another significant difference between the two applications is that in atomized liquids, for direct transition each liquid fragment is usually converted into

one Lagrangian droplet with equal volume, while in cavitating flows, each Eulerian structure is actually a cloud of bubbles or a bubbly mixture and its properties (e.g. density) are not equal to the pure vapour (dispersed phase) properties. Therefore, the cavity might be replaced by a group of smaller bubbles (instead of one larger bubble) in such a way that the properties of the combined bubble group are equal to the corresponding values of the old Eulerian cavity. A key factor in developing hybrid solvers is the correct and smooth transition between Lagrangian and Eulerian structures. When an Eulerian mixture structure is transformed to a Lagrangian bubble or vice versa, as the related transport equation to track the structure is changed, a wrong transition process may cause sudden changes in mixture properties and lead to spurious numerical pulses in the domain.

An example of a hybrid cavitation model is the work of Hsiao et al. [25] who coupled a Lagrangian discrete singularities model with an Eulerian level set approach. In that model, natural free field nuclei and solid boundary nucleation are used in the representation of cavitation inception and enable the capture of the sheet and cloud dynamics. The method is in good agreement with 2D experiments in terms of sheet cavity length and shedding frequency, however it has not been validated with a 3D case and according to the authors, the result do not yet show clear cloud shedding which is assumed to be due to inadequate grid resolution. Numerical stability and compatibility between the two frameworks can be major issues in developing hybrid cavitation models. Hence, the earlier models include simplifications in the Lagrangian representation and the Eulerian-Lagrangian transition algorithm. Some of these issues which cause spurious pressure pulses and other physical inconsistencies in the flow field are addressed in the current study.

1.3 OBJECTIVES OF THE STUDY

Considering the described capabilities and limitations of different models in the previous section, the main objective of this study is to develop a hybrid mixture-bubble model in OpenFOAM that is capable in representing cavitation phenomenon with extensive range of length scales from large sheet and cloud cavities that may fully cover a device surface to sub-grid micro-bubbles. To fulfil this objective, the following steps have been taken in this thesis.

- Development of a Lagrangian bubble model in OpenFOAM: There is no Lagrangian cavitation model in the OpenFOAM code, and the first step is to develop such a model by implementing a basic available Lagrangian library in a suitable continuum flow solver in the code. Then, the Lagrangian library needs to be improved to solve for the bubble dynamics and consider the bubble effect on the continuum flow field. A necessary step in this part is to implement and improve the general Rayleigh-Plesset equation in calculating the bubble size variations. Other necessary improvements in this part are correcting the bubble-wall boundary condition in OpenFOAM and taking into account the bubble-bubble interactions and bubble break-up.

- Comparing different cavitation models: A general description of the limitations of different models was given in §1.2. However, to have a further understanding of each model behaviour and to find the potential area of improvements for the Eulerian and Lagrangian parts of the hybrid model, the performance of the three types of the cavitation models should be further investigated. In this regard the EoS, TEM and Lagrangian models are compared in the simulation of benchmark test cases. Such a study also verifies the implementation of the Lagrangian model in OpenFOAM.

- Coupling of the Eulerian mixture model with the Lagrangian bubble model: To develop the main hybrid solver, the Lagrangian bubble and Eulerian mixture models should be coupled in OpenFOAM and a transition algorithm should be defined to transform the small collapsing cavities from the Eulerian framework to the Lagrangian one and also to transform large Lagrangian structures to the Eulerian framework. This step is similar to the work of Vallier [26], in turn inspired by the study of Tomar et al. [23].

- Realizable improvements of the hybrid mixture-bubble model: As will be explained in the following chapters, the initial algorithm for the coupling of the mixture and bubble models should be improved further. The improvements are needed to have a physically compatible transition between Eulerian and Lagrangian frameworks, and to consider the bubble contribution in the continuous flow field and mixture properties.

- Verification and validation of the solver: To validate the hybrid model performance in representing various cavities of different scales and to evaluate the new submodels, the solver will be applied to a 3D real problem. In order to make the solver applicable to real scale flows, it is also needed to make a number of additional adjustments in the numerical code. Parallelization of the solver, using bubble parcels and optimizing the Lagrangian models to reduce the computational costs are a few examples of such adjustments.

- Experimental study of a multi-scale cavitating flow: Apart from developing the numerical model, in this study we need a 3D test case for validation of the solver. Such a test case should include different features of a typical cavitating flow such as cavitation inception, the development of small vapour structures to large structures as well as shedding and collapse of cavitating clouds. Although there are various experimental cases in literature, here we need a test case with satisfactory records and detailed analysis of the cavitation field and it should specifically include the mentioned features at different length scales. Therefore, a series of experimental tests is performed in this study to find a suitable case. As will be shown, the cavitating flow around a sharp edge bluff body is used as the required test case. Based on the earlier experience, the cavity structures around this bluff body can be highly erosive at high flow rates and it is desirable to obtain a detailed analysis of this complex flow from numerical simulation.

1.4 COMPOSITION OF THE THESIS

This thesis is mainly based on four journal papers and one conference paper which can be considered as subsequent blocks in the development and validation of the hybrid model. There are also other relevant studies and investigations which are not reported here, but that have been published in separate papers. The thesis was initiated by developing a general solver through the coupling of the Eulerian mixture model in OpenFOAM with a simple Lagrangian model. After that, the Lagrangian model was improved with implementation of various submodels to consider different phenomena in bubble dynamics. This step was followed by a set of experimental tests to learn the multi-scale flow physcis and to find a suitable 3D test case for validation of the hybrid solver. Afterwards, the solver was optimized further by additional refinements to make it applicable to 3D real scale flows. Finally it was applied to a relevant test case from the earlier experiments.

In Paper I, the basic principles of the hybrid solver is presented. The general algorithm for the transformation of cavity structures between the Eulerian and Lagrangian frameworks is described with some improvements in defining the parameters of new Lagrangian bubbles, and revising the Eulerian governing equations in order to take into account bubble effects on the continuous flow field.

In Paper II, the initial development of the Lagrangian model is introduced and the model performance in bubble collapse prediction is verified with two benchmark test cases. Here the primary submodels of the Lagrangian approach are presented and among them is the introduction of a localized form of the Rayleigh-Plesset equation, which considers the local pressure effect on bubble dynamics. The paper also includes a comparison between the Lagrangian model with two Eulerian mixture models for further understanding of the capabilities and limitations of each approach. Following this analysis, Paper III includes a further investigation in the Eulerian transport equations and finite mass transfer model.

Paper IV mainly presents the experimental part of this research. In the experiments the cavitating flow around a surface mounted cylinder is investigated. In this part different features of the cavitating flow around the cylinder are investigated in detail to have a comprehensive understanding of the flow physics. Besides, the paper includes the preliminary results of the Eulerian mixture model.

In Paper V, the final hybrid model is described with detailed description of its various submodels and the solution algorithm. In this paper, the model performance in representation of multi-scale cavities is validated with a test case from the experimental study and the obtained results are compared with the corresponding ones from the Eulerian model.

Chapter 2 provides an overview of the hybrid model and the coupling of the Eulerian and Lagrangian frameworks. In chapter 3, a summary of the numerical models and the governing equations are presented. Subsequently, the experimental tests are described in chapter 4. The content of the papers are summarized in chapter 5, with more focus on the results. Finally, the conclusions are summarised in chapter 6, followed by recommendations for future studies in chapter 7.

2

Methodology

This chapter gives a general description of the hybrid solver and explains how the Eulerian mixture and Lagrangian bubble models are coupled in the solution algorithm.

In Figure 2.1, the general solution algorithm is described schematically. In the hybrid model, the large vapour structures are modelled through the Eulerian mixture approach and the small-scale structures are represented as discrete parcels of bubbles. The governing equations of the continuous flow field (i.e. the conservation equations for mass and momentum) is the same for both and the main difference is in the tracking of the cavity structures. Here, the cavities are categorized as Eulerian structures and Lagrangian bubbles to be tracked in the corresponding framework. The categorization into Lagrangian and Eulerian groups is done based on the relative size of each cavity with the local grid size of the discretized domain. If a cavity is large enough to be resolved by a sufficient number of computational cells, then it is tracked in the Eulerian framework, otherwise it is treated as parcels of Lagrangian bubbles. Furthermore, since the volume of each cavity can change in the flow, at each time step the small Eulerian structures or large Lagrangian cavities may be transformed from one framework to the other.

In the Eulerian modelling, the mixture of vapour and liquid phases is treated as a single mixture fluid, where the continuity equation and one set of momentum equations for the mixture are solved. We here consider an incompressible flow and a transport equation model (TEM), motivated by the balance of computational cost and model accuracy for the large-scale applications as will be shown later, but a similar framework can be developed for compressible flows. By solving the transport equation, we obtain the liquid volume fraction (denoted by α) which is used to update the mixture properties (e.g. density).

In the Lagrangian modelling, the cavities are treated as discrete parcels of bubbles in an ambient Eulerian continuous flow. At each time step, the Eulerian continuity and momentum equations are solved first, then the bubbles are tracked

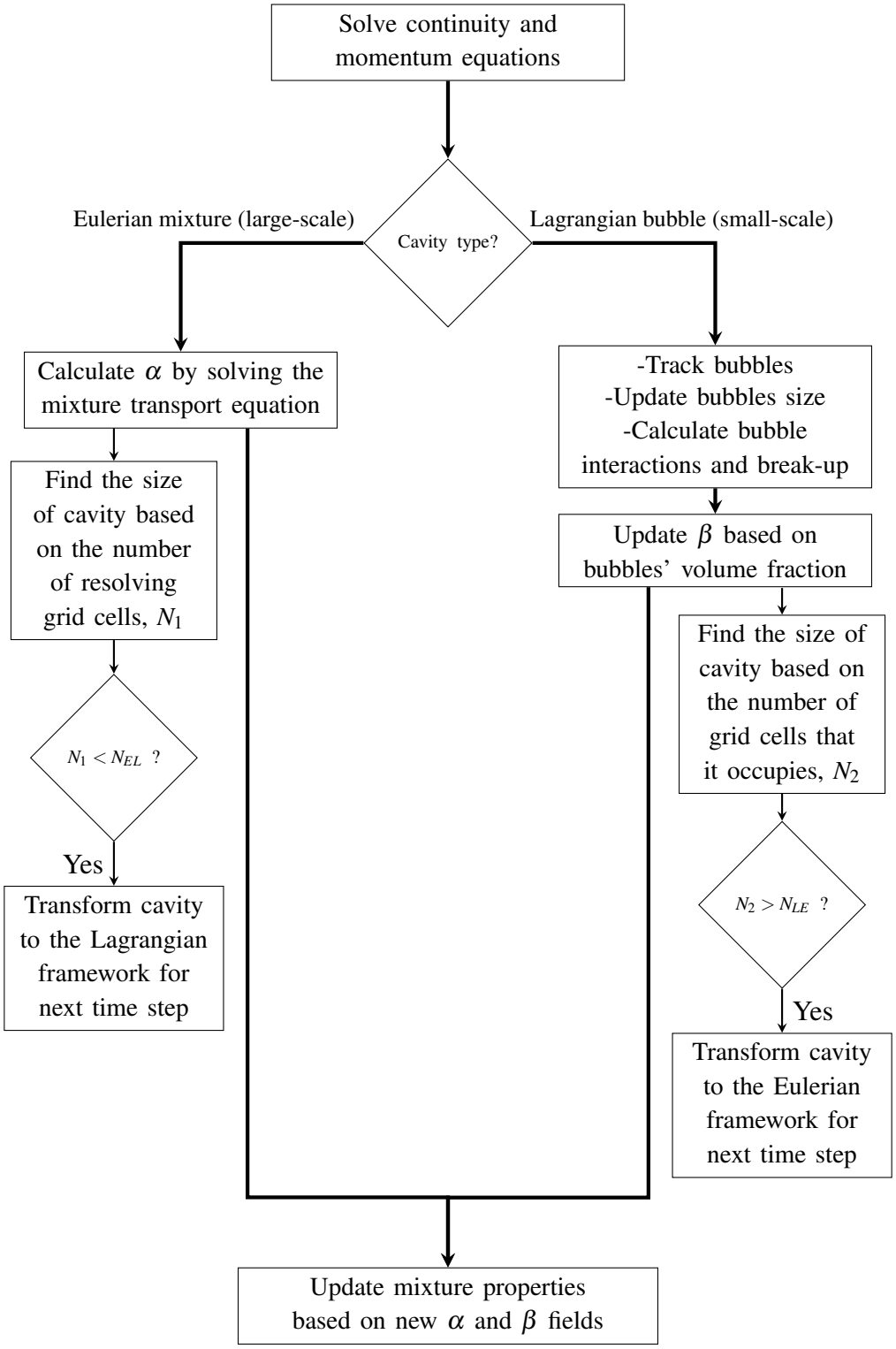

Figure 2.1: Schematic description of a time step in the general solution algorithm.

by solving a set of ordinary differential equations along the bubble trajectory. Afterwards the bubble dynamics is updated and its interactions with the other cavities is modelled. Then the Eulerian vapour fraction is updated based on the bubbles new positions and radii. The vapour fraction is used to update the mixture properties (e.g. density) and consider the bubble effect on the ambient flow.

For updating the mixture properties based on liquid and vapour fractions, it is important to note that the vapour content of each cell is represented by either Eulerian or Lagrangian models. In other words, it is assumed that Eulerian and Lagrangian cavities do not co-exist in the same cell. To distinguish between the obtained volume fraction from bubble distribution with the one that is calculated from the Eulerian transport equation (α), we use another variable, β, for Lagrangian cavities. In a similar way, β is used to update the properties of the liquid-vapour mixture in the Eulerian governing equations, as will be explained in detail in §3.2. It should also be noted that since in the hybrid model we have both Eulerian and Lagrangian cavities, the governing equations of the continuous flow field should be revised accordingly to include both α and β and it is described in §3.3.

Furthermore, the solution algorithm needs a procedure for transition of small Eulerian cavities to the Lagrangian framework and vice versa. This procedure includes two parts: a criterion to determine when a cavity should be transformed from one framework to the other; and an algorithm which specifies how such a transition should be performed. For the transition criterion, similar to the other hybrid models (e.g. [26], [27] and [28]), we consider two threshold numbers related to the size of the cavity in relation to the grid: N_{EL} for Eulerian to Lagrangian transformation and N_{LE} for Lagrangian to Eulerian transformation (Figure 2.1). If an Eulerian cavity is represented by an enough number of computational cells which is larger than N_{EL}, then it is kept in the Eulerian framework, otherwise it is determined to be unresolved and transformed to a group of Lagrangian bubbles. On the other hand, if a Lagrangian cavity (i.e. a cloud of Lagrangian bubbles) is large enough and occupies more than N_{LE} cells, then it is transformed to the Eulerian framework, as it can be resolved by sufficient number of cells; otherwise it is kept in the Lagrangian framework. The two threshold numbers are different and $N_{LE} > N_{EL}$ so that when a small Eulerian cavity is transformed to a group of Lagrangian bubbles, its (possibly) fast collapse and rebound process can be modelled using the Lagrangian equations, instead of having a quick transformation back to the Eulerian framework.

How the Eulerian-Lagrangian transition is performed is in basic principles similar to the algorithm developed by Vallier [26]. This algorithm was also followed by Lidtke [27] for prediction of radiated noise and recently by Peters and el Moctar [28] for estimation of cavitation-induced erosion. It can be shown that the algorithm, in its original form, does not follow the conservation laws for mass, momentum and kinetic energy in a cavitating flow. This, in turn, can induce spurious pressure pulses and vapour generation and lead to solution instability and numerical errors in noise and erosion estimation. These issues are explained in detail

in Paper I. To address these issues, the algorithm is improved in the current study. The main improvements include: transforming each Eulerian cavity to a group of smaller bubbles (instead of one large bubble) in such a way that the properties of the combined bubble group are equal to the corresponding values of the Eulerian structure; considering the bubble contribution in the liquid-vapour mixture to avoid sudden unrealistic variations in the mixture properties; and considering the bubble effect in the mass transfer rate to avoid spurious vapour generation. The bubble effect is taken into account through the introduction of the β parameter, and the revision of the governing equations as will be described in the following chapter. The current algorithm is compatible with the flow physics and it follows the conservation laws.

In addition, the algorithm is improved further to be applicable in real case 3D flows. In the current hybrid model, the bubble size is updated by solving a new localized form of the Rayleigh-Plesset equation which takes into account the local pressure effect on bubble dynamics. Another improvement is the correction of bubble wall boundary condition which is important in the transport of large bubbles. Furthermore, the bubble-bubble interaction is improved both to follow the physical conservation laws and to considerably increase the computational efficiency. The other new contributions are revising the void handling scheme and implementing another submodel to consider the bubble break-up due to the flow turbulence and velocity fluctuations. Detailed description of the stated features is given in the following chapter.

All of the numerical models have been developed in OpenFOAM (Open Source Field Operation and Manipulation) [29]; for the Lagrangian and hybrid models this involves improving the interPhaseChangeFOAM solver and coupling it with a Lagrangian library, which is an improved version of an available Lagrangian model in OpenFOAM. OpenFOAM is an open source C++ package to model and simulate fluid dynamics and continuum mechanics. More details about this package can be found in [30], [31] and [32]. In this work, the OpenFOAM version v1806 is used.

3

Numerical models

This chapter presents the details of the numerical models including the developed and applied submodels. In the first two sections, the Eulerian and Lagrangian models and their governing equation are described. Then, in the third section, it is explained how these two models are coupled with each other in the hybrid model and how the governing equations are revised accordingly. Finally, a brief description of the numerical test cases is given in the last section.

3.1 HOMOGENEOUS MIXTURE MODEL

In the transport equation model, the vapour and liquid phases are treated as a single mixture fluid and mass and linear momentum are conserved in the flow. Also, the liquid-vapour mixture is represented by a transport equation for the liquid volume fraction, where the mass transfer between the phases is defined as an explicit source term to the equation and surface tension effects are assumed small and are neglected. Here, the flow is considered as incompressible and isothermal, motivated by the balance of computational cost and model accuracy for the intended applications, but a similar framework can be developed for compressible flows. Therefore, the governing equations in this model are the continuity and Navier-Stokes equations, as well as a transport equation to represent the mass conservation for the liquid/vapour phase and to calculate the liquid-vapour interface. The equations are Favre-averaged and then spatially filtered to perform LES. Turbulence is modelled using an Implicit Large Eddy Simulation (ILES) approach.

Although the pure liquid and pure vapour are considered as incompressible, the mixture density varies based on volume fraction of the immiscible phases and hence the unfiltered continuity equation is written by

$$\frac{\partial \rho_m}{\partial t} + \frac{\partial (\rho_m u_i)}{\partial x_i} = 0, \tag{3.1}$$

where u_i is the flow velocity vector and ρ_m denotes the mixture density, and the unfiltered momentum equation is

$$\frac{\partial(\rho_m u_i)}{\partial t} + \frac{\partial(\rho_m u_i u_j)}{\partial x_j} = -\frac{\partial p}{\partial x_i} + \frac{\partial \tau_{ij}}{\partial x_j} + \rho_m g_i. \tag{3.2}$$

In the implicit LES (ILES) approach the numerical dissipation is considered enough to mimic the subgrid terms [33, 34]. In the above equation, p is the static pressure, g_i is the gravity vector and τ_{ij} is the stress tensor which is defined as

$$\tau_{ij} = \mu_m \left(\frac{\partial u_i}{\partial x_j} + \frac{\partial u_j}{\partial x_i} - \frac{2}{3}\frac{\partial u_k}{\partial x_k}\delta_{ij} \right), \tag{3.3}$$

where δ_{ij} is the kronoker delta, and μ_m is the mixture dynamic viscosity. Assuming homogeneous flow, the mixture density and viscosity are obtained using the linear relations as

$$\rho_m = \alpha\rho_l + (1-\alpha)\rho_v, \tag{3.4}$$

$$\mu_m = \alpha\mu_l + (1-\alpha)\mu_v. \tag{3.5}$$

In the above relations ρ_l is the liquid density and ρ_v is the vapour density, while μ_l and μ_v denote liquid and vapour dynamic viscosities, respectively. α is the liquid volume fraction that specifies the relative amount of liquid in a control volume, e.g. a computational cell. In the current model, the evolution of the volume fraction is calculated by solving a transport equation given as

$$\frac{\partial \alpha}{\partial t} + \frac{\partial(\alpha u_i)}{\partial x_i} = \frac{\dot{m}}{\rho_l}, \tag{3.6}$$

where $\dot{m}$ is the rate of mass transfer between phases and is obtained from a finite mass transfer (FMT) model. Using Eqs. 3.4 and 3.6, Eq. 3.1 may be rewritten as

$$\frac{\partial u_i}{\partial x_i} = (\frac{1}{\rho_l} - \frac{1}{\rho_v})\dot{m}. \tag{3.7}$$

The RHS term denotes the effect of vaporization and condensation. For incompressible pressure-based solvers it is more convenient to use the velocity divergence relation, rather than the complete form of the continuity equation (Eq. 3.1). Therefore, the main governing equations in this model are Eqs. 3.2, 3.6 and 3.7.

To close the above set of equations, the mass transfer rate, $\dot{m}$, should be specified using an FMT model. In this study, the Schnerr-Sauer model [15] is used, which has been proven in earlier studies to give satisfactory results with reasonable computational cost (see e.g. [7]). The vaporization and condensation rates are then given by

$$\begin{aligned}
\dot{m}_c &= C_c\alpha(1-\alpha)\frac{3\rho_l\rho_v}{\rho_m R_B}\sqrt{\frac{2}{3\rho_l|p-p_{threshold}|}}\max(p-p_{threshold},0),\\
\dot{m}_v &= C_v\alpha(1+\alpha_{Nuc}-\alpha)\frac{3\rho_l\rho_v}{\rho_m R_B}\sqrt{\frac{2}{3\rho_l|p-p_{threshold}|}}\min(p-p_{threshold},0),
\end{aligned} \tag{3.8}$$

where $\dot{m}_c$ and $\dot{m}_v$ are the rates of condensation and vaporization, respectively, and $\dot{m} = \dot{m}_c + \dot{m}_v$. In the above equations, R_B and α_{Nuc} are the generic radius and volume fraction of bubble nuclei in the liquid, while C_c and C_v are the condensation and vaporization rate coefficients in OpenFOAM [29]. Based on the obtained results in Papers II and III, using larger empirical constants leads to more satisfactory results, which has been reported by Schenke and van Terwisga [35] as well. In Eq. 3.8, $p_{threshold}$ is a threshold pressure at which the phase change is assumed to happen, usually considered as the vapour pressure of the fluid, which is 2320 Pa in the current simulations. Finally, the liquid and vapour densities are assumed to be $\rho_l = 998.85$ kgm^{-3} and $\rho_v = 0.02$ kgm^{-3}, and the corresponding dynamic viscosity values are set as $\mu_l = 0.00109$ kgm^{-1}s^{-1} and $\mu_v = 1.39 \times 10^{-5}$ kgm^{-1}s^{-1}.

From the equations it is seen that the mass transfer rate model neglects the effects of dissolved gas pressure, surface tension and viscous force.

3.2 Lagrangian bubble model

As stated before for this model, at each time step, the Eulerian equations are solved first, then the bubbles are tracked by solving a set of ordinary differential equations along the bubble trajectory, after which the Eulerian vapour fraction is updated based on the new bubble positions and radii. The Eulerian governing equations are the continuity and Navier-Stokes equations as described for the finite mass transfer model (Eqs. 3.7 and 3.2). To avoid high computational costs, instead of modelling all of the bubbles, parcels of them are tracked. Each parcel represents a number of identical non-interacting bubbles which are assumed to be spherical.

3.2.1 Bubble effect on the Eulerian flow field

Since the dispersed (bubble) phase in the cavitating flow is locally dense, and it has properties quite different from liquid properties, the bubbles have considerable effects on the ambient flow field (similar to the Eulerian cavities) as well as other bubbles. Thus, both the bubble-bubble and bubble-flow interactions should be considered in the model. In this study, the bubble effect on the ambient flow field is considered through implementing its volume fraction contribution in the calculation of mixture properties and phase change rate (Eqs. 3.4, 3.5 and 3.8), similar to the described finite mass transfer model (§3.1). In this approach, the flow is considered as a single fluid mixture of continuous liquid and disperse bubbles, and the Eulerian governing equations are similar to the homogeneous mixture model. However, the liquid volume fraction of each cell is obtained from bubble cell occupancy, instead of solving the scalar transport equation (Eq. 3.6). Therefore, for such a Lagrangian model the mixture properties are given as

$$\rho_m = \beta\rho_l + (1-\beta)\rho_v, \qquad \mu_m = \beta\mu_l + (1-\beta)\mu_v, \tag{3.9}$$

where β is the liquid volume fraction and simply $1-\beta$ is the bubble volume fraction in the computational cell. It should be mentioned that the continuity

equation source term is obtained using the Schnerr-Sauer model (Eq. 3.8), similar to the mixture model. It is possible to calculate the phase change source term from bubble size and distribution variation directly, however as the main intention is to use the Lagrangian approach coupled to a FMT based model, the Schnerr-Sauer model is preferred here.

The remaining part is to calculate vapour volume fraction from the instantaneous bubble sizes and locations. In the general case a cavitating bubble may grow and occupy more than one grid cell. If we assume that a bubble parcel i is occupying N_{cell} cells, then the parcel void fraction in cell j can be estimated as

$$v_{i,j} = \frac{1}{V_{cell,j}} \left(\frac{4}{3} \pi n_i R_i^3 \right) f \left(\frac{|\mathbf{x}_{i,j}|}{R_i} \right), \tag{3.10}$$

in which R_i is the bubble radius, n_i is the number of bubbles that the parcel represents, $f\left(\frac{|\mathbf{x}_{i,j}|}{R_i}\right)$ is the Gaussian distribution function and $|\mathbf{x}_{i,j}|$ is the distance between the cell and parcel centre. The cells that are included in the formula are located around the bubble host cell and they are partially or fully occupied by the parcel, and the parcel volume is not distributed over the unoccupied neighboring cells. The standard deviation of the distribution function is calibrated so that 99.7% of the parcel volume is distributed within the $|\mathbf{x}_{i,j}| < R_i$ range. Since Eq. 3.10 does not necessarily guarantee that the parcel volume is conserved, the void fraction should be corrected as

$$v_{i,j}^c = v_{i,j} \frac{\frac{4}{3} \pi n_i R_i^3}{\sum_{k=1}^{N_{cell}} v_{i,k} V_{cell,k}}. \tag{3.11}$$

Finally as a cell can be occupied by $N_b \geq 1$ parcels, the vapour void fraction of cell j is the summation of all bubble void fractions given as

$$1 - \beta_j = \sum_{i=1}^{N_b} v_{i,j}^c = \sum_{i=1}^{N_b} v_{i,j} \frac{\frac{4}{3} \pi n_i R_i^3}{\sum_{k=1}^{N_{cell}} v_{i,k} V_{cell,k}}. \tag{3.12}$$

In cavitating flows, bubbles may experience significant pressure drop within a short distance which can result in a substantial growth. Therefore, it is possible that some parcels get larger than the fine hosting cells. One of the inherent assumptions in Lagrangian modelling is that the dispersed-phase volume fraction should not be too high. Theoretical problems arise in the limit of very low values of β. Another situation with high Lagrangian vapour fraction is in the locally dense regions where a cell hosts a large number of bubbles. When the presence of Lagrangian bubbles approaches the packing limit, overpacking should be prevented, otherwise it can lead to unphysical results and risk of crashing the solver. In this study, the maximum value of bubble volume fraction is limited to 0.64 (or $\beta_{min} = 0.36$), which is a relevant number corresponding to random close packing

limit of monodispersed spheres. Therefore, the bubble volume fraction in each computational cell is calculated using Eq. 3.12, and for the overpacked cells the excessive volume fraction is distributed to the neighboring cells. It should be mentioned that this case does not happen frequently in the hybrid solver, since dense Lagrangian cavities are usually transformed to the Eulerian framework, as will be shown later. In the extreme case when a bubble is larger than the surrounding cells, it is enough to spread its volume over an approximate radial distance of $1.16R = \left(\frac{1}{0.64}\right)^{\frac{1}{3}} R$. Distribution of the bubble volume over only the neighboring cells that are occupied by the cavitating bubbles gives a more precise estimation of the real concentration field as compared to some of the earlier studies (e.g. [25, 18, 26]) in which the bubble volume is spread within a larger radial distance, e.g. $3R$.

3.2.2 Bubble equations of motion

The Lagrangian equations for tracing bubbles are given by

$$\begin{aligned} \frac{d\mathbf{x}_b}{dt} &= \mathbf{u}_b, \\ m_b \frac{d\mathbf{u}_b}{dt} &= \mathbf{F}_d + \mathbf{F}_l + \mathbf{F}_a + \mathbf{F}_p + \mathbf{F}_b + \mathbf{F}_g, \end{aligned} \tag{3.13}$$

where $\mathbf{x}_b$ and $\mathbf{u}_b$ denote the bubble position and velocity vectors, and m_b is the mass of the bubble. The RHS of the second equation includes various force components exerted on the bubbles. The listed forces in the equation are, from left to right, sphere drag force, lift force, added mass, pressure gradient force, buoyancy force, and gravity. These forces are given as

$$\begin{aligned} \mathbf{F}_d &= \frac{3}{4} C_D \rho \frac{m_b}{\rho_b d_b} (\mathbf{u} - \mathbf{u}_b) |\mathbf{u} - \mathbf{u}_b|, \\ \mathbf{F}_l &= 6.46 C_l \rho \frac{m_b}{\rho_b} (\mathbf{u} - \mathbf{u}_b) \times (\nabla \times \mathbf{u}), \\ \mathbf{F}_a &= \frac{1}{2} \rho \frac{m_b}{\rho_b} \left(\frac{D\mathbf{u}}{Dt} - \frac{d\mathbf{u}_b}{dt} \right) \\ \mathbf{F}_p &= \frac{m_b}{\rho_b} \nabla p, \\ \mathbf{F}_b &= -m_b \frac{\rho}{\rho_b} \mathbf{g}, \\ \mathbf{F}_g &= m_b \mathbf{g}. \end{aligned} \tag{3.14}$$

In these relations, ρ_b and d_b are the bubble density and diameter and ρ in the density of the surrounding fluid. Also, C_D and C_l are the drag and lift force coef-

ficients, respectively.

Another fundamental assumption in classical Lagrangian methodologies is that the particles' (or bubbles') dimensions under consideration should be smaller than the characteristic size of the Eulerian mesh. In fact, the maximum particle size should be such that $5 \sim 10\ d_{max} < L$, where L is the characteristic cell size. This assumption can be violated in cavitating flows, due to the combination of dense grids and the growth of bubbles in low pressure regions. In order to circumvent this limitation, in Eq. 3.14, instead of interpolating the Eulerian values at the bubble centre, the corresponding values are averaged along the surface of a larger and concentric imaginary sphere. This sphere has a diameter of $5d_b$. The forces typically depend on the bubble size, and hence correct estimation of bubble dynamics is of great importance.

3.2.3 Bubble dynamics

The classical Rayleigh-Plesset equation can reasonably well estimate the collapse and growth rate of a single bubble in an infinite domain [1]. However due to inherent assumptions of the equation, it cannot be applied, in its original form, to complex and real problems in which bubbles are surrounded by other cavity structures and flow boundaries. In this study, a localized form of the Rayleigh-Plesset equation is derived to consider local pressure effect on bubble dynamics. This equation is given as

$$\rho_l \left(\frac{1}{2} R\ddot{R} + \frac{17}{32} \dot{R}^2 \right) = p_v + p_{g0} \left(\frac{R_0}{R} \right)^{3k} - p_{2R} - 4\mu_l \frac{\dot{R}}{R} - \frac{2\sigma}{R}, \tag{3.15}$$

where R is the bubble radius with $\dot{R}$ and $\ddot{R}$ denoting its first and second temporal derivatives, respectively. The summation of the first two terms on the RHS is the bubble pressure, where p_v is the vapour pressure and $p_{g0} \left(\frac{R_0}{R} \right)^{3k}$ is the dissolved gas pressure with p_{g0} and R_0 representing the initial equilibrium gas pressure and radius, respectively. The exponent, k, is set to 1 if the bubble content behaves isothermally and to γ (gas polytropic constant) if the bubble radius varies adiabatically. p_{2R} is the surface-average pressure of the mixture over a concentric sphere with radius $2R$, representing the local pressure around the bubble. Finally the last two terms represent the viscous stress and surface tension stress on the interface, with σ denoting the surface tension coefficient. Further details of this equation and its derivation can be found in Paper II.

For solving Eq. 3.15, all of the parameters should be specified. The surrounding fluid properties (σ, μ, γ and ρ) are either constant values or surface-average interpolated at $5R$, as explained before. Also, the vapour pressure, p_v, is considered as the liquid-vapour saturation pressure at the flow temperature. Then, the only unknown term is the dissolved gas pressure which is a function of the initial (or reference) radius, R_0, and gas pressure, p_{g0}, of the bubble. By assuming that

each bubble origins from a nucleus which has been in equilibrium condition far away from the cavitation zone, the following relation between the initial gas pressure and bubble radius is obtained from the original form of the Rayleigh-Plesset equation,

$$p_{g0} = p_\infty - p_v + \frac{2\sigma}{R_0}, \tag{3.16}$$

where p_∞ is the far-field pressure, assumed to be 101325 Pa. In this study, it is assumed that the radius of the assumed nuclei is 1 μm, which corresponds to $p_{g0} =$ 242 kPa. However, it is possible in the solver to adjust these parameters based the experimental data of water quality, if available. Also, in the hybrid model, when an Eulerian cavity is transformed to a Lagrangian bubble, initial values of $\dot{R}$ and $\ddot{R}$ are obtained based on the volume variation rate of the old Eulerian vapour, as will be described later.

3.2.4 Bubble-bubble collision

For the four-way coupling, the method for how bubble–bubble collisions are handled is a critical issue. There are two fundamental parts to the calculation of bubble collisions, the incidence of collision and the outcome of collision. In the current Lagrangian model we track parcels directly, rather than using representative distribution functions. Therefore, the bubble collisions are handled using a deterministic algorithm similar to the work of Breuer and Alletto [36], in which the trajectories of every two particles i and j are checked to investigate their possible collision along their path line. The algorithm is first explained for colliding bubbles and later it is extended for parcel collisions. To find the collision possibility between each bubble and other bubbles, instead of having a loop over all of the other bubbles, which is computationally expensive, we use a more efficient method and detect the bubble-bubble collision by a faster algorithm based on the "cell occupancy" concept. The cell occupancy concept and the detection of possible collisions between the bubbles close to each other are described in detail in Paper V.

The outcome of collision is assumed to be a function of two time-scales, the bubbles interaction time, t_i, and the liquid film drainage time, t_d. According to Kamp et al. [37], these time scales are given by

$$\begin{aligned} t_i &= \frac{\pi}{4}\left(\frac{\rho {D_{eq}}^3}{6\sigma}\right)^{1/2}, \\ t_d &= k\frac{\rho V_{rel} {D_{eq}}^2}{8\sigma}, \end{aligned} \tag{3.17}$$

where, V_{rel} is the relative velocity between the two bubbles in the normal direction, and $D_{eq} = \frac{4R_1R_2}{(R_1+R_2)}$ is the equivalent diameter of the bubbles with radii R_1 and R_2. Also, k is a correction factor which accounts for various approximations made

in deriving the expressions for t_i and t_d, and is set to 2.5 [37]. The coalescence probability is expressed as

$$P_{coal} = e^{-t_d/t_i}. \tag{3.18}$$

Then a random number is sampled from uniform distribution function. If this number is larger than the coalescence probability, then the bubbles are assumed to bounce back after collision; otherwise, they are considered to coalesce. For the first scenario, the bubble normal velocities after collision are calculated as

$$u_{1n}^{+} = \frac{m_1 u_{1n}^{-} + m_2 u_{2n}^{-} - \varepsilon m_2 (u_{1n}^{-} - u_{2n}^{-})}{m_1 + m_2}, \qquad u_{2n}^{+} = \frac{m_1 u_{1n}^{-} + m_2 u_{2n}^{-} + \varepsilon m_1 (u_{1n}^{-} - u_{2n}^{-})}{m_1 + m_2}, \tag{3.19}$$

where m_1 and m_2 denote the bubbles' mass, u_{1n}^{-} and u_{2n}^{-} are their relative normal velocities before collision, and ε is the restitution coefficient which is set to 0.8 in this study. Here, it is assumed that the bubble tangential velocity does not change, implying no friction between the colliding pair. If the bubbles coalesce after collision, then we need to estimate the properties of the new bubble. Following [38], this process is assumed to satisfy the following conservation relations,

$$V_1 + V_2 = V_3, \tag{3.20}$$

$$\dot{V}_1 + \dot{V}_2 = \dot{V}_3, \tag{3.21}$$

$$p_{B1} V_1 + p_{B2} V_2 = p_{B3} V_3, \tag{3.22}$$

$$\mathbf{x}_1 V_1 + \mathbf{x}_2 V_2 = \mathbf{x}_3 V_3, \tag{3.23}$$

$$\mathbf{u}_1 V_1 + \mathbf{u}_2 V_2 = \mathbf{u}_3 V_3, \tag{3.24}$$

where index 3 identifies the properties of the third bubble and V_i is the bubble volume whose temporal variation rate is represented by $\dot{V}_i = 4\pi R^2{}_i \dot{R}_i$. Eqs. 3.20 and 3.21 conserve the vapour volume and kinetic energy, respectively. From these equations R_3 and $\dot{R}_3$ are obtained. Eq. 3.22 conserves the internal energy of the vapour inside the bubble. From this relation the new bubble pressure, p_{B3} is calculated, which in turn is used to estimate the dissolved gas pressure (p_{g3}), while p_v is constant. Finally, Eqs. 3.23 and 3.24 maintain a constant centre of mass and the momentum, respectively, and from them we estimate the new bubble centre ($\mathbf{x}_3$) and velocity ($\mathbf{u}_3$) vectors.

As stated earlier, Eqs. 3.17-3.24 describe the interactions between a pair of bubbles. For a pair of bubble parcels, we assign an equivalent radius to each bubble group that is represented by a parcel. The equivalent radius is simply given as

$$R_{eqv,i} = \left(\frac{3}{4\pi} V_{tot,i} \right)^{\frac{1}{3}} = n_i{}^{\frac{1}{3}} R_i, \tag{3.25}$$

where $V_{tot,i}$ and n_i are the total volume vapour and number of bubbles that are represented by a specific parcel i. Hence the equivalent diameter of the bubble pair in Eq. 3.17 should be calculated based on the parcel equivalent radii (i.e. $D_{eq} = \frac{4R_{eqv,1}R_{eqv,2}}{R_{eqv,1}+R_{eqv,2}}$). Furthermore, in Eqs. 3.19-3.24 the bubble mass (m_i) as well as bubble volume and its temporal rate (V_i and $\dot{V}_i$) should be replaced by the corresponding values of the bubble group.

3.2.5 Bubble break-up

The non-uniform pressure distribution and hydrodynamic forces in the surrounding fluid cause bubble deformation which can lead to break-up. The break-up process can have different mechanisms regarding the governing physical process. The main mechanisms that have been studied extensively in literature are: turbulent fluctuation and collision; viscous shear stress; shearing off process; and interfacial instability [39]. From these mechanisms, bubble break-up due to turbulent fluctuation along the surface or by collision with eddies have been investigated most extensively. Lau et al. [39] showed that various reported bubble break-up criteria can be written in terms of a critical Weber number, *We*, which can be regarded as a dimensionless ratio between the inertial force (which causes deformation) and the surface tension (which tends to restore the bubble sphericity). For turbulent flow around a bubble, it can be defined as

$$We = \frac{\rho \overline{\left(u_i' u_i'\right)_{d_p}} d_p}{\sigma}, \tag{3.26}$$

where $\overline{\left(u_i' u_i'\right)_{d_p}}$ is the mean square velocity difference over a distance equal to bubble diameter. The criterion for bubble break-up is usually defined as a critical value for *We* number. For instance, Giannadakis et al. [19] used a critical value of 12, which is similar to what Lau et al. [39] has derived for spherical bubbles.

Similar to most break-up models reported in the literature, we assume binary break-up in the current study. The size of daughter bubbles is determined by the break-up volume fraction, f_{bv}. In a recent study, Hoppe and Breuer [40] derived a relation for critical *We* number based on the break-up volume fraction, given as

$$We_{crit} = 12\frac{d_p}{d_s} = 12 f_{bv}^{-\frac{1}{3}}, \tag{3.27}$$

where d_s denotes the small daughter bubble diameter. The ratio $f_{bv}^{-\frac{1}{3}}$ has a minimum value of $0.5^{-\frac{1}{3}} = 1.26$ for break-up into two equally-sized daughter bubbles. In this case the critical *We* number has a minimum value 15.12 which is the closest one to the corresponding value mentioned above. Other daughter size distributions would corresponds to larger critical Weber numbers which means a larger turbulent kinetic energy to break the deformed bubbles. In this study, the bubble parcels are assumed to break-up into equally sized daughter parcels and the *We* number is considered to be 15.12.

To calculate the properties of the daughter bubbles, it is assumed that the break-up process follows similar conservation relations that was used for the description of bubble coalescence process.

3.2.6 Bubble-wall interaction

In this study, the wall boundaries are considered to be rigid and it is assumed that a bubble collides with a wall when the distance between its centre to the nearest

wall face becomes equal or less than its radius. Also, it is assumed that after collision a bubble bounces from the wall.

An important issue in the tracking of Lagrangian bubbles, that should be considered in numerical modelling, is the relative sizes of bubbles and grid cells. Sometimes (e.g. due to significant pressure drop) a bubble may grow and occupy several cells. In OpenFOAM, and some other widely used numerical codes, when a bubble approaches a wall, the wall boundary condition is applied correctly only if the bubble size is smaller than the cell edge in the wall normal direction. If a bubble is larger than this limit, the bubble-wall collision is not detected. In the current study the bubble wall boundary condition in OpenFOAM is improved to model the large bubble wall collision appropriately.

3.3 THE MULTI-SCALE HYBRID MODEL

In this model, the large vapour structures are modelled through the Eulerian mixture approach, and the small-scale structures are represented as discrete bubbles. The governing equations of the continuous flow field are similar to the previous models (i.e. Eqs. 3.2 - 3.8) and the main difference is in the tracking of the cavity structures. Here, the cavities are categorized as Eulerian structures and Lagrangian bubbles to be tracked in the corresponding framework.

As mentioned in Chapter 2, the categorization of the structures into Lagrangian and Eulerian groups is done based on the relative size of each cavity to the local grid size of the discretized domain. If a cavity is large enough to be resolved by an enough number of computational cells, then it is tracked in the Eulerian framework, otherwise it is treated as parcels of Lagrangian bubbles. Furthermore, since the volume of each cavity can change in the flow, at each time step the small Eulerian structures or large Lagrangian cavities may be transformed from one framework to the other. In the previous sections the cavity volume fraction is specified by either the α or β parameters, but here, the governing equations should be revised to consider both Lagrangian bubbles (β) and Eulerian cavities (α) together in the solution algorithm. Besides that, another algorithm needs to be defined for the transformation of Eulerian cavities to Lagrangian bubbles and vice versa.

3.3.1 Eulerian-Lagrangian transition

During transition, cavities are transformed directly from one framework to the other. At each time step, small Eulerian cavity structures that are not resolved by sufficient number of computational cells, are transformed to Lagrangian bubbles. Eulerian cavity structures are detected in the flow domain by the hosting cells liquid volume fraction which is less than 1. Thus, to remove an Eulerian structure, the corresponding liquid volume fraction of the respective cells (α) needs to be set equal to 1. This transition is shown schematically in Figure 3.1 for a simple

2D grid. The grid cells that have Eulerian cavities are coloured blue with $\alpha < 1$. Two of the cavities are resolved only by four cells and they are replaced by Lagrangian bubbles. Also, if a Lagrangian cavity later becomes large enough, it is transformed back to a Eulerian structure by deleting the corresponding bubbles and setting a new α value in the occupied cells. In addition, if each Lagrangian bubble approaches a large Eulerian structure, it is transformed to the Eulerian framework and becomes a part of that large cavity.

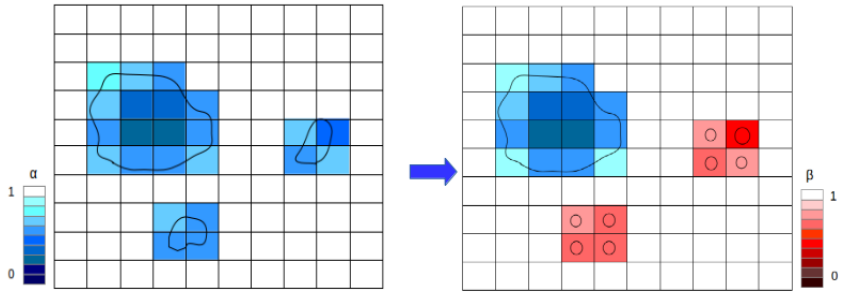

Figure 3.1: Transition of small Eulerian cavities to Lagrangian bubbles.

When bubbles replace a cavity cloud by setting the α value to 1 without considering the effect of new bubbles in the mixture properties (as described in §3.2.1), the sudden change in the α value will cause a jump in the values of the mixture properties, ρ_m and μ_m, (based on the Eqs. 3.4 and 3.5) as well as the mass transfer source term (Eq. 3.8). Such significant changes can cause spurious numerical pressure pulses which may have considerable unrealistic effects on the flow field and the resulting erosion/noise prediction. The same scenario can occur when a Lagrangian cavity is transferred to an Eulerian cloud (see Eq. 3.9). Therefore, the governing equations of the continuous flow should be written based on a new parameter that is conserved during the transition process. The improved relations for mixture properties and mass transfer rate are given as

$$\begin{aligned} \rho_m &= \alpha\beta\rho_l + (1-\alpha\beta)\rho_v, \\ \mu_m &= \alpha\beta\mu_l + (1-\alpha\beta)\mu_v, \end{aligned} \tag{3.28}$$

$$\begin{aligned} \dot{m}_c &= C_c\alpha\beta(1-\alpha\beta)\frac{3\rho_l\rho_v}{\rho_m R_B}\sqrt{\frac{2}{3\rho_l|p-p_{threshold}|}}\max(p-p_{threshold},0), \\ \dot{m}_v &= C_v\alpha\beta(1+\alpha_{Nuc}-\alpha\beta)\frac{3\rho_l\rho_v}{\rho_m R_B}\sqrt{\frac{2}{3\rho_l|p-p_{threshold}|}}\min(p-p_{threshold},0). \end{aligned} \tag{3.29}$$

Here, the earlier α (or β) terms are replaced by their product $\alpha\beta$. During the Eulerian to Lagrangian transition, the new value of β in the cavity hosting cells is the same as the old value of α and vice versa. Therefore, both α and β have similar sudden changes while their product $\alpha\beta$ does not change during the Eulerian-Lagrangian transition. In the cells containing bubbles, where $\alpha = 1$, $\alpha\beta$ has the same value as β and in Eulerian cavity zones where $\beta = 1$, $\alpha\beta$ is equal to α. It is important to note that in each computational cell the vapour structure should be represented in either Eulerian or Lagrangian framework. Therefore, in cells containing bubbles the generation of Eulerian cavities should be avoided by revising

the α transport equation source term as

$$\frac{\partial \alpha}{\partial t} + \frac{\partial (\alpha u_i)}{\partial x_i} = \frac{\dot{m}}{\rho_l} * \mathrm{pos}(\beta - 1). \tag{3.30}$$

When there is a bubble in a cell, β is less than 1, therefore the $\mathrm{pos}(\beta - 1)$ equals zero and no cavity is generated in the cell. To the best of the author's knowledge, the revision of governing equations (Eqs. 3.28-3.30) is missing in the earlier hybrid models of this type. An exception is the recent study by Peters and el Moctar [28], in which the Lagrangian bubbles contribution in the mixture properties is taken into account. Here, the modelling is developed one step further by considering the bubble effects in the mass transfer rate and α transport equations.

Another important point in the transition process is the specification of new bubble properties. The small Eulerian cavities, that are transformed to the Lagrangian framework, are usually sparse clouds with low vapour concentration. Therefore, it is not realistic to replace the whole structure with one single bubble of pure vapour but one should use a cloud of smaller bubbles. The small bubbles can have different distributions in size and position, and to decrease the computational expenses it is suggested to keep the number of bubbles as low as possible. Besides that, to ensure local conservation of vapour volume in each computational cell, the vapour content of each individual cell is replaced by relative individual parcels whose diameter is less than the minimum edge of the cell, Figure 3.1. Then the vapour volume of each cell is replaced by at least one parcel and the number of bubbles for that parcel is defined based on the vapour volume conservation. When bubble radius and the number of bubbles for each parcel are determined, other Lagrangian properties can be specified based on the conservation relations and equilibrium equations. The bubble growth rate, $\dot{R}$, and its temporal rate, $\ddot{R}$, are obtained from the corresponding values for the Eulerian cavity as

$$\begin{aligned} \dot{R}_i &= \frac{\dot{V}_{v,j}}{n_i q_j 4\pi R_i^2}, \\ \ddot{R}_i &= \frac{\ddot{V}_{v,j} - n_i q_j 8\pi R_i \dot{R}_i^2}{n_i q_j 4\pi R_i^2}, \end{aligned} \tag{3.31}$$

where q_j is the number of parcels in cell j, $\dot{V}_{v,j}$ denotes the growth rate of Eulerian vapour volume in the cell and $\ddot{V}_{v,j}$ is its temporal rate. A correct initialization of $\dot{R}$ and $\ddot{R}$ is an important point which is not taken into consideration in the earlier hybrid cavitation models.

After explaining different aspects of the Eulerian to Lagrangian transition, the overall algorithm of this process can be summarised now. In the first step, all of the cavity structures in the flow domain are detected. Next, the number of computational cells that represent each structure are counted. If the number of cells is less than a threshold value, denoted as N_{EL}, it is decided that the relative structure is not represented by sufficient number of grid cells. Then, for each cavity that is not well resolved, Algorithm 1 is followed.

Also, if a Lagrangian bubble collides with a large Eulerian cavity, or it becomes large enough to be resolved by sufficient number of cells, it will be transformed to an Eulerian structure by deleting the bubble, while in the host cell β is set to 1 and $\alpha = \beta_{old}$. In this study, the transition criterion is based on a threshold number of grid cells. In the solver implementation, the user can set two parameters, N_{EL} and N_{LE}, which are the threshold numbers of cells, based on which an Eulerian structure is transformed to a group of Lagrangian bubbles and vice versa, respectively.

Algorithm 1 Eulerian to Lagrangian transition algorithm

1: Create a list of cell labels $\{\text{cell } j \ , \ j = 1 : J\}$, that are hosting the cavity structure.

2: **for** `j=1:J` **do**

3: Evaluate the cavity volume $V_{v,j}$ and its temporal derivatives, $\dot{V}_{v,j}$ and $\ddot{V}_{v,j}$.

4: Find the minimum edge length of the cell, $\Delta_{min,j}$.

5: Specify the number of parcels in the cell, q_j. Then the number of bubbles for each parcel and their radii are calculated as

$n_i q_j \frac{4}{3}\pi {R_i}^3 = V_{vapour,j}$,
$R_i \leq \Delta_{min,j}$.

6: **for** `i=1:`q_j **do**

7: Find the parcel position vector $\mathbf{x}_i$ in cell j:
The positions vectors are q_j points in the cell volume with uniform distribution.

8: Set the bubble velocity, $\mathbf{u}_i$, equal to the Eulerian mixture velocity in the cell, $\mathbf{u}_j$ and its density, ρ_i equal to ρ_v.

9: Find $\dot{R}_i$, $\ddot{R}_i$ and p_{g0} from Eqs. 3.31 and 3.16.

10: Inject the bubble parcel.

11: **end for**

12: Remove the Eulerian cavity of the cell by setting $\alpha_j = 1$.

13: **end for**

As mentioned earlier, the hybrid solver is developed based on the coupling of the presented Lagrangian model with the the solver *interPhaseChangeFoam* in OpenFOAM. In this solver the pressure (continuity) and velocity (momentum) equations are coupled using a PIMPLE algorithm [29]. This algorithm is a merge

of the SIMPLE [41] and PISO algorithms, where the PISO loop is complemented by an outer iteration loop, see e.g. [42] for different ways to merge PISO and SIMPLE procedures. In the current study, at each time step, four outer SIMPLE loops are performed, and in each SIMPLE loop, four PISO pressure correction loops are performed. The final solution algorithm of the hybrid solver is depicted in Figure 3.2.

3.4 NUMERICAL TEST CASES

In order to verify the implemented solver and to validate different parts of the developed model, the following numerical tests have been performed. The obtained results are discussed briefly in the following chapter, and in this section the numerical settings are described.

3.4.1 Single bubble collapse

The collapse of a single bubble is a benchmark test case that has been widely used for primary validation of different numerical models in the literature. Here the collapse of a vapour bubble in an infinite medium with atmospheric pressure is simulated and the effects of viscosity, non-condensible gas, and surface tension are ignored. This problem is also known as the *Rayleigh bubble collapse* and can be solved analytically up to the collapse time. Here, we consider the case where initial bubble radius is 0.4 mm and the flow is assumed to be initially at rest. The initial pressure around the bubble has a Laplacian distribution. The far field boundary is located at 0.5 m from the bubble centre, with a fixed atmospheric pressure (10^5 Pa) and zero gradient conditions for liquid volume fraction and velocity. Considering the spherical symmetry of the flow field, only an asymmetric wedge mesh with an angle of five degrees is created. The total domain is discretized with 5,000 cells, including 100 points in the radial direction. The initial bubble is well resolved by 20 cells in the radial direction and 50 cells in the circumferential direction. This test case was simulated using three different models: the Eulerian TEM model, the Lagrangian model, and an equilibrium mixture model to investigate the capabilities and limitations of each approach. For the Lagrangian model simulation, instead of liquid volume fraction initialization, a 0.4 mm bubble is injected at the first time step and the corresponding liquid volume fraction is calculated from bubble cell occupancy. The time step is set to 5×10^{-9} s for the incompressible simulations and 1×10^{-10} s (corresponding to CFL number of 0.32) for the compressible simulation. The simulations are performed for larger time steps and coarser grids as well, to study the relative effects. Furthermore, for the TEM and Lagrangian models, different empirical constants (C_c and C_v) of the mass transfer rate, between 1 to 10^4, are examined to find optimal values. A description of the equilibrium model can be found in Paper II.

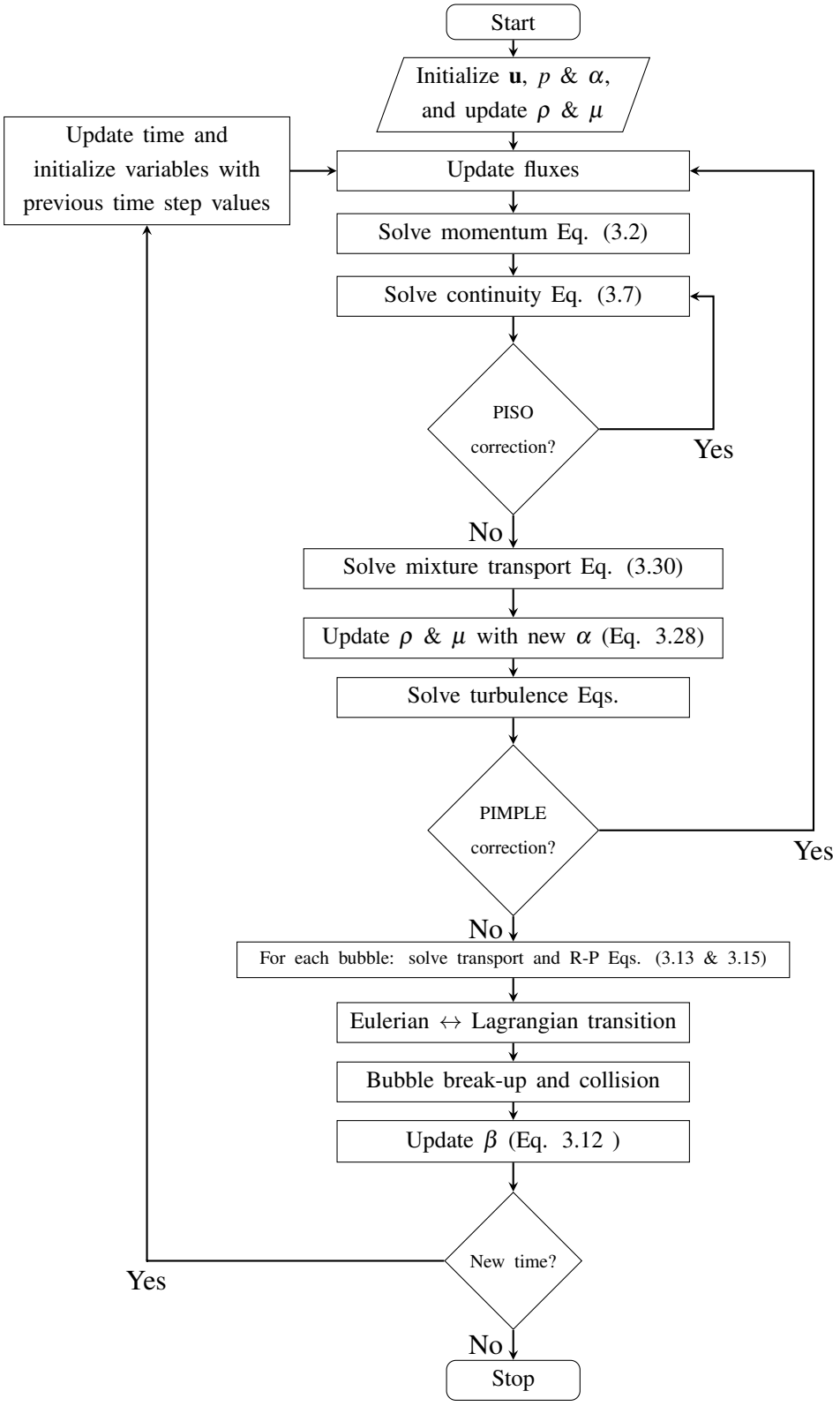

Figure 3.2: Hybrid solver algorithm.

3.4.2 Collapse of a bubble cluster

The above-mentioned three models were also applied for the simulation of the collapse of a cluster of bubbles over a flat wall. Here, the bubble dynamics is affected by the collapse of the surrounding bubbles as well as the near wall influence. In the current study, the bubble cloud which was previously defined by Schmidt et al. [43] is used. This cloud consists of 125 spherical vapour bubbles with a radius distribution ranging from 0.70 mm to 1.64 mm with non-uniform distribution. The average radius of the bubbles is 0.95 mm and they have a minimum distance of 0.2 mm to avoid intersection. Also, they have larger concentration and radii around the center of the cloud. The overall cloud is located in a small liquid-filled cubic domain of $20 \times 20 \times 20$ mm^3 and has a total volume fraction of 5.8 %. The cubic domain, itself, is located in a larger rectangular domain of $4 \times 4 \times 2$ m^3 and the bottom faces of the two domains are coplanar. The bubble distribution inside the inner domain is depicted in Figure 3.3.

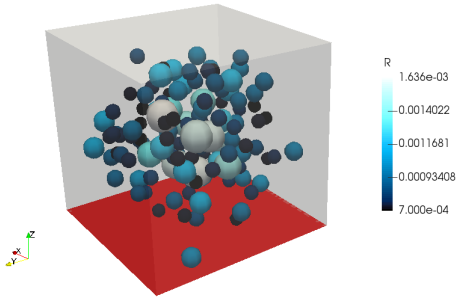

Figure 3.3: Distribution of 125 spherical non-intersecting bubbles within the small cubic domain of 20^3 mm^3 over a flat wall (red surface). This small domain is inside a larger outer domain of $4 \times 4 \times 2$ m^3 (not shown here).

The fluid domain is assumed to have a stationary initial condition with a uniform temperature of 293 K. The initial pressure inside the bubbles is set equal to the vapour pressure and in the surrounding liquid it is assumed to have a Laplacian distribution, which is reasonable for a stationary condition. The coplanar bottom faces of the domain are defined as impermeable walls and other outer faces are considered as far-field boundaries with constant pressure of 40 bar and no gradient of other flow parameters.

To discretize the bubble cloud, the small domain consists of 55^3 Cartesian structured cells with the numerical resolutions (Δ_{CFD}) of 0.36 mm, and it is equivalent to Grid 3 in the work of Schmidt et al. [44, 43]. In this discretization, the smallest bubbles are represented by about 32 cells and the largest ones are discretized by more than 400 cells, which approximately corresponds to $0.2 < \Delta/R < 0.5$; it is thus coarse compared with the resolutions studied for the single bubble collapse. The time step of the simulations is 3.9×10^{-8} s corresponding to a CFL number (for compressible solution) of 0.7. Finally, in order to measure

the imposed pressure of the collapsing bubbles on the bottom wall, one pressure transducer is located at the center of the bottom face. This transducer covers an area of 1×1 cm^2.

3.4.3 2D hydrofoil

To verify the proposed improvements in the Eulerian-Lagrangian transition algorithm, the performance of the new multi-scale model is examined for the cavitating flow over a hydrofoil. In Figure 3.4, two cavity structures with different length scales are shown over the suction side of a 2D hydrofoil. The large structure should be kept in the Eulerian framework while the smaller one is a candidate to be transformed to the Lagrangian framework. It is worth mentioning that for 2D simulations, in the third direction one grid cell with a length of 1 is used, as OpenFOAM uses 3D meshes. Following this approach, 2D bubbles are defined as circular cylinders whose longitudinal length are aligned in the third direction. And each cylinder has a length of 1, similar to the cell length.

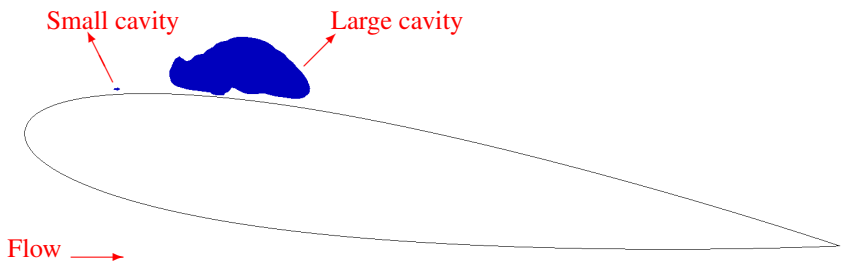

Figure 3.4: Cavities with different length scales over the 2D hydrofoil.

3.4.4 Cavitating flow around a surface-mounted cylinder

This test case is used for validation of the hybrid model. Here, the cavitating flow around a bluff body is studied. The bluff body has a finite length with semi-circular cross section and is mounted on a surface in the throat of a converging-diverging channel. Detailed information about the test conditions as well as the flow geometry and dimensions is given in the next chapter along with a description of the experimental test series. The computational domain is depicted in Figure 3.5, including the domain inlet and outlet boundaries as well as the pressure probe locations and the small cylinder in the converging-diverging section of the channel. In the figure, w denotes the channel width normal to the plane, which is constant in the whole domain. At the inlet a constant volume flow rate condition is applied for velocity while the pressure gradient is set to zero. At the outlet a constant pressure is set such that the probe pressure p_2 is equal to the equivalent

experimental value, while zero gradient condition is set for velocity. Furthermore, a no-slip condition is applied on all solid boundaries including the bluff body.

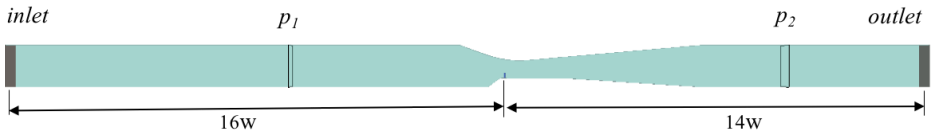

Figure 3.5: Computational domain of the bluff body test case.

To discretize the flow domain a structured mesh consisting of 4.8 million cells is used. The mesh is non-uniform with finer cells around the cylinder and near the walls. If we consider the area from the start of the sloped wall to the end of the flat plate behind the cylinder as the critical area, 2.5 million cells of the generated grid are located in this zone. The first cells on the cylinder and the surrounding walls around it have a height of 0.015 mm which leads to a y^+ value below 7. The time step is set between 1×10^{-7} s and 5×10^{-7} s which yields a maximum Courant number of $0.3 - 1.5$. Also, turbulence is modelled using Implicit Large Eddy Simulation (ILES) approach. The physical constants and numerical parameters of the hybrid model simulations are summarized in Table 3.1. A range of values for the threshold numbers, N_{EL} and N_{LE}, are used as explained in Chapter 5.

Table 3.1: Hybrid model constants for the bluff body simulations

Parameter	Value	Parameter	Value
C_c	30	$C_{v'}$	30
$p_{threshold}$ (Pa)	2320	n_0 (m^{-3})	10^{10}
d_{Nuc} (m)	10^{-5}	μ_v ($kg.m^{-1}.s^{-1}$)	1.39×10^{-5}
μ_l ($kg.m^{-1}.s^{-1}$)	0.00109	ρ_v ($kg.m^{-3}$)	0.02
ρ_l (kgm^{-3})	998.85	ρ_b ($kg.m^{-3}$)	0.02
R_0 (m)	10^{-6}	p_{g0} (Pa)	2.42×10^5
p_v (Pa)	2320	ε	0.8
γ	1.4	k	2.5
σ ($kg.s^{-2}$)	0.072	Interaction dist. (m)	0.0005
N_{EL}	7-50	N_{LE}	14-100

4

Experimental test

In the experimental tests, the cavitating flow around a bluff body is studied. The bluff body has a finite length and is mounted on a surface in the throat of a converging-diverging channel. This set-up creates various 3D flow structures around the body, from cavitation inception to super cavities, at high Reynolds numbers ($Re = 5.6 \times 10^4 - 2.2 \times 10^5$) and low cavitation numbers ($\sigma_d = 0.56 - 1.69$). This study is an attempt to understand different features of the cavitating flow due to the cylinder effect, with a special objective to find a suitable multi-scale cavitating case. The multi-scale test case is then used for both validating the numerical model and investigating some of the flow characteristics at different scales of a cavitation problem.

The bluff body is a flat-front semi-circular cylinder which is mounted on a surface in the throat of a converging-diverging channel. The mounted cylinder and a simple sketch of the test section are depicted in Figure 4.1. The channel (Figure 4.1(b)) has a rectangular cross section with dimensions of 74×54 mm^2 which is contracted to a section of 25×54 mm^2 through a curved profile upper wall and a simple 45° slope on the lower wall, while the channel width is constant everywhere. The cylinder has a diameter of 5 mm and a length of 9.65 mm and it is put at the end of the lower slope and after that, there is a flat plate with dimensions of 106×54 mm^2. The flat side of the cylinder is facing upstream and at the attachment of the flat plate and the sloped wall, there is a small backward facing step with a height of 0.5 mm. The cavitation number is defined as

$$\sigma_d = \frac{p_2 - p_v}{\frac{1}{2}\rho u_{th}^2}, \tag{4.1}$$

where p_2 is the downstream pressure, p_v is the vapor pressure and u_{th} is the area-averaged velocity of the flow at the throat of the converging-diverging section without cylinder. The downstream pressure is measured at a distance of 500.5 mm after the bluff body. The pressure probe location can be seen in Figure 4.1(b).

The experimental data have been captured using high-speed imaging for a vast range of cavity patterns.

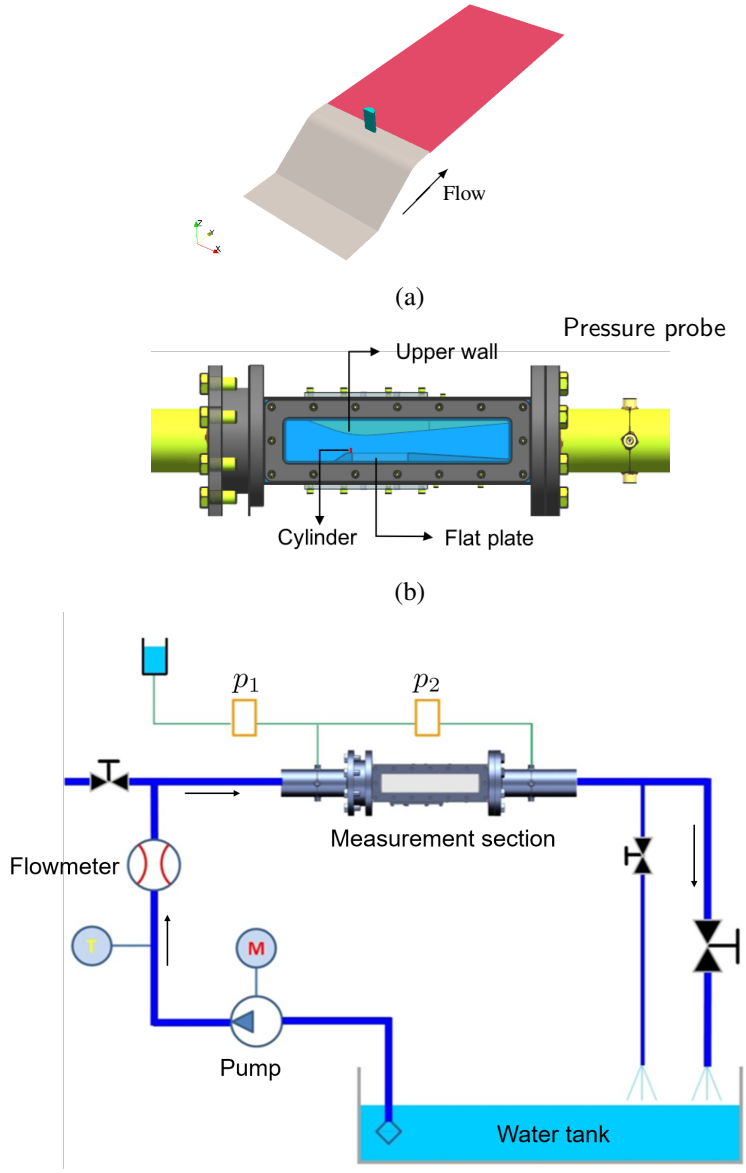

Figure 4.1: Test case: (a) Lower wall and bluff body; (b) Measurement section; (c) Schematic overview of the experimental facility indicating different components (dimensions not to scale).

Figure 4.1(c) shows the experimental facility. The upstream length available for development is more than 100D, in order to have a fully-developed turbulent flow entering the test section. The feeding line of the experimental setup is a circular tube with a diameter of 114.3 mm; however, it is transformed into a rectangular

section (74×54 mm^2) through a converging tube at 140 cm before the main test section. After the test section, the pressure in the flow is recovered in a pressure recovery section. At the end of the pressure recovery section, a valve is present to vary the global static pressure of the system. There are two outflow pipes, however only the second pipe is used during the tests. The flow can be visualized through the sidewalls, which are made of Polymethyl methacrylate (PMMA). A high-speed camera (Phantom v411) with a field of view of 640×232 pixels was used for imaging. Two light sources from the front and an LED panel behind the measurement section were used to illuminate the cavity. The camera was placed at an angle of 32° to the horizontal to capture the cavity.

Further information about the set-up as well as the experimental procedure can be found in Paper IV. Details of different test conditions are given in Table 4.1. In this table, the non-dimensional numbers are based on the average velocity at the channel throat (u_{th}), the average downstream pressure (p_2) and the cylinder diameter (D) as the reference values. Also, p_1 is the upstream pressure of the test section with σ_u as the corresponding cavitation number, Q is the volume flow rate and Δp denotes the pressure drop over the test section.

Table 4.1: Test cases

No.	$p_1(bar)$	$Q(m^3/s)$	$\Delta p(bar)$	Re ($\times10^4$)	σ_u	σ_d
-1	1.122	0.015	0.065	5.6	1.79	1.69
0	1.248	0.0175	0.087	6.5	1.47	1.37
1	1.403	0.0201	0.114	7.4	1.26	1.16
2	1.646	0.0237	0.157	8.7	1.066	0.964
3	1.803	0.0257	0.184	9.5	0.994	0.893
4	2.0	0.0282	0.219	10.4	0.923	0.822
5	2.36	0.032	0.279	11.8	0.844	0.744
6	3.36	0.0408	0.441	15.1	0.738	0.641
7	4.25	0.0471	0.608	17.4	0.705	0.604
8	6.22	0.0582	1.068	21.5	0.675	0.559

The experimental tests were performed at Andritz Hydro Laboratory in Vevey, Switzerland, and in a collaboration between the thesis author, Mr. Saad Jahangir (TU Delft) and Dr. Magdalena Neuhauser (Andritz Hydro).

5

Summary of results

This chapter gives summaries of the appended papers, outlining their aims and major results.

5.1 PAPER I

Realizability improvements to a hybrid mixture-bubble model for simulation of cavitating flows

As stated in previous chapters, the hybrid model is inspired by the study of Vallier [26]. The aim of this paper is to improve the original coupling algorithm between the Eulerian and Lagrangian frameworks and to revise the governing equations in order to avoid spurious pressure pulse and vapour generation.

In the original model, when an Eulerian vapour structure is replaced by a bubble, the liquid volume fraction value (α) in the respective cells is set to 1. This sudden change will cause a jump in the values of the mixture properties, ρ_m and μ_m (see Eqs. 3.4 and 3.5), as well as the mass transfer rate, $\dot{m}$ (Eq. 3.8). Such significant changes in the flow properties and the continuity equation source term can cause spurious numerical pressure pulses which may have significant unrealistic effects on the flow field. For example, these pulses can decrease the local pressure in the cavitating region which leads to generation of new cavities.

In order to avoid these problems and create a smooth and physically compatible transition, three improvements have been developed: considering the bubbles' contribution in the mixture framework (in addition to the Eulerian cavities); a careful introduction of bubbles in relation to cell size and mixture distribution; and attention to mass transfer in the presence of discrete bubbles. As a results, the original governing equations (Eqs. 3.4-3.8) are revised to Eqs. 3.28-3.30. Also, the transition algorithm is improved as schematically depicted in Figure 3.1.

To verify the new corrections, an example problem of a small cavity in the flow over a 2D foil (Figure 3.4) was simulated. Figure 5.1 compares the im-

proved model with the original one based on the minimum flow pressure, the local vapour volume and number of Lagrangian bubbles for a few time steps after an Eulerian to Lagrangian transition. Figure 5.1(a) shows significant pressure pulses (large negative values) from the original model while the minimum pressure by the improved model is constant and equal to the saturation vapour pressure. After an Eulerian to Lagrangian transition, no Eulerian vapour should be generated in the transition area as the vapour phase is represented by Lagrangian bubbles. In Figure 5.1(b), however, we see that using the original model spurious vapour is generated in the domain. As the new Eulerian cavities are small, they are transformed to Lagrangian bubbles and the number of Lagrangian bubbles increases in the subsequent time steps, which is not realistic. In the same figure, it is seen that these issues are avoided by the new formulation.

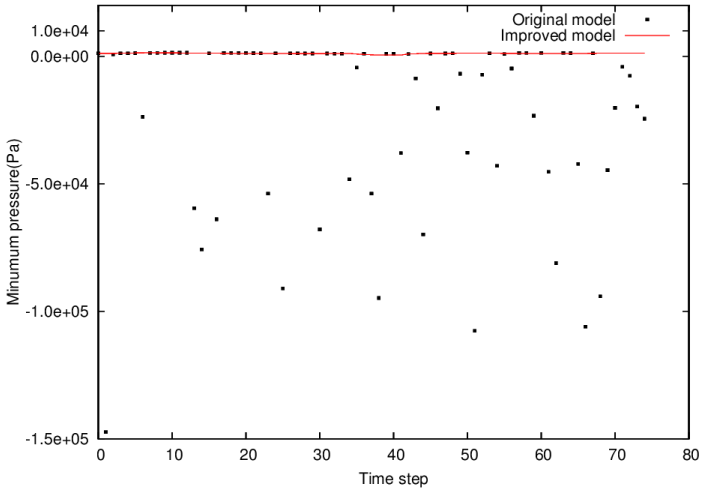

(a)

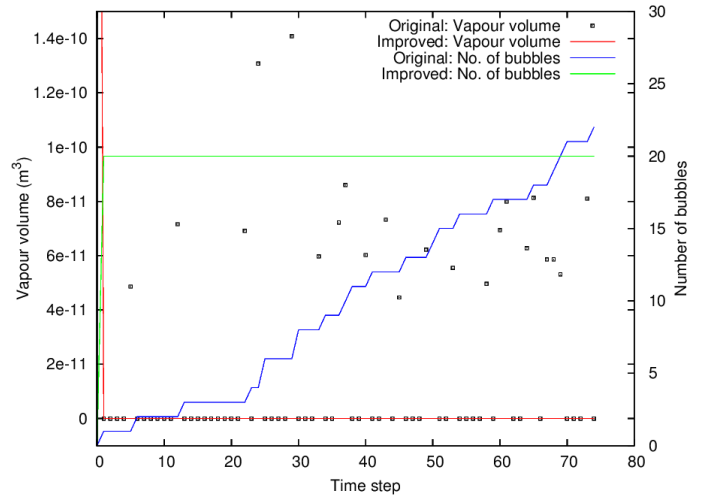

(b)

Figure 5.1: The measured minimum flow pressure (a), Eulerian vapour volume and number of bubbles (b) after an Eulerian-Lagrangian transition.

5.2 Paper II

A comparative study between numerical methods in simulation of cavitating bubbles

This paper has three objectives: to verify the implemented Lagrangian model in OpenFOAM, to validate the new improvements in solving bubble dynamics, and to investigate the performance of two Eulerian mixture models and a Lagrangian bubble model in predicting the collapse of cavitating bubbles. The Eulerian models include a compressible equilibrium model (EoS) and an incompressible transport equation model (TEM). Also, in the Lagrangian model, the bubble deformation is calculated using both the original and improved forms of the Rayleigh–Plesset equation to investigate the effect of local pressure in estimation of bubble collapse rate (Eq. 3.15).

The models are applied to two benchmark test cases: the collapse of an isolated single bubble, and the collapse of a bubble cluster (Figure 3.3). In the first case, the obtained results from all numerical models are compared to the analytical solution. As an example, in Figure 5.2 the estimated pressure profile from the TEM model is depicted for five different instances (t/τ) during the collapse of a single bubble. The horizontal axis is the non-dimensional radial distance from bubble centre while the vertical axis is the non-dimensional pressure. The plot corresponds to the empirical model constants (C_c and C_v) of 10^4 and shows that the pressure profile can be represented by this model with a rather certain accuracy. Further results of this test case (presented in the paper) shows that all the three models can capture the collapse rate appropriately and the pressure profile accuracy can be improved if the bubble radius is calculated/resolved more accurately. Furthermore, some numerical pulses are detected in the compressible simulation, and for the incompressible simulations the empirical constants should be sufficiently large. Using the Lagrangian model, the bubble radius can be well estimated with coarser grid and larger time steps. As an example, Figure 5.3 compares the estimated pressure profile of the Lagrangian model with two time steps and using the new localized form of the R-P equation. In the figure, the results of the main time step ($\Delta T = 5 \times 10^{-9}$ s, used in the main simulations for all models) is compared with those of a larger time step ($\Delta T = 1 \times 10^{-7}$ s). As shown, even with 20 times larger time steps, the pressure profiles are well-estimated with rather similar pressure peaks, and no numerical pulse.

Figure 5.4 shows the Lagrangian model results in estimations of the collapse rate of a cluster of bubbles with non-uniform distributions in both position and radius. Here, the compressible EoS results are used as the reference solution (black line). The plot shows the Lagrangian model results for three different forms of the Rayleigh-Plesset equation: the new localized R-P (blue line), the original R-P with the infinity pressure (p_∞) set equal to the farfield pressure of 40 bar (red line) and p_∞ set equal to the pressure at bubble interface (green). The last case is similar to the R-P equation that is used is some of the earlier Lagrangian and hybrid models in literature (e.g. [19, 25]). It is seen that while the obtained

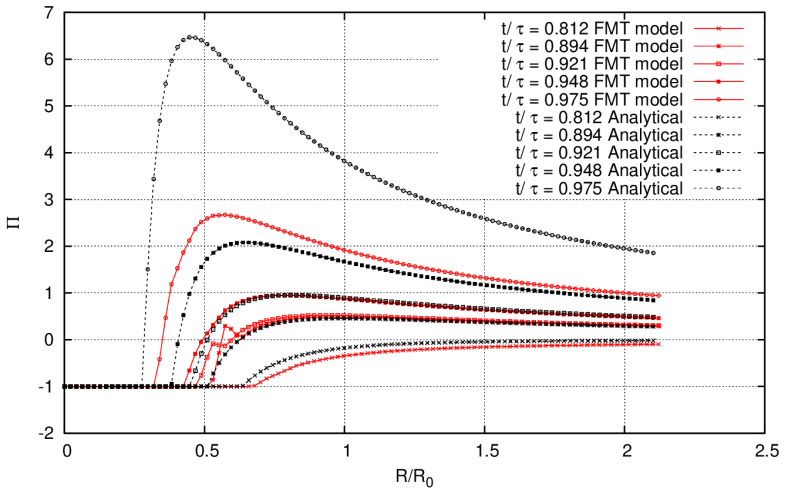

Figure 5.2: Comparison of TEM model pressure distribution with analytical data for the collapse of a single isolated bubble.

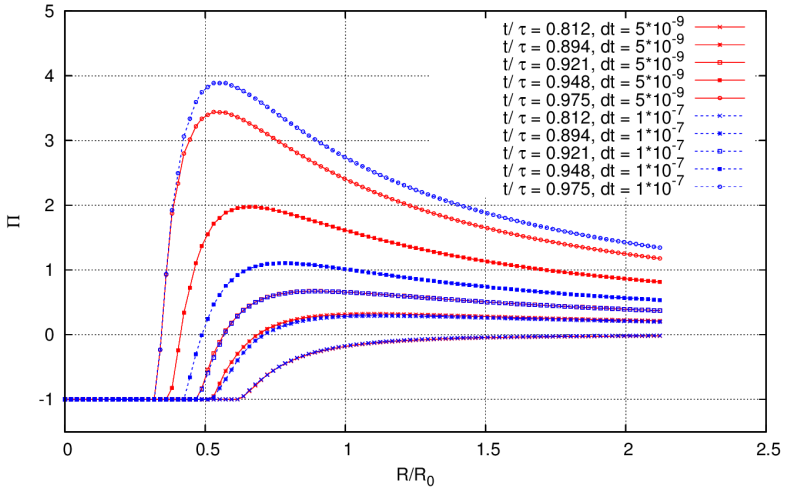

Figure 5.3: Time-step dependency of the Lagrangian model results based on the localized R–P equation.

profile by the local R-P equation is very similar to the reference solution, using the two forms of the original R-P equation leads to significant overestimation or underestimation of the collapse rate.

In summary, the results show that both mixture models estimate a diffusive liquid–vapour interface and to have a more precise representation they need finer grids. Furthermore, they have issues with spurious pressure pulses for a single bubble collapse. These issues are avoided with the Lagrangian model, even with coarser grids and larger time steps. Also, in the general cases that a bubble is surrounded by other cavity structures or confined by flow boundaries and the surrounding flow field is not symmetrical, the new R-P formulation gives a much more appropriate representation of the bubble dynamics.

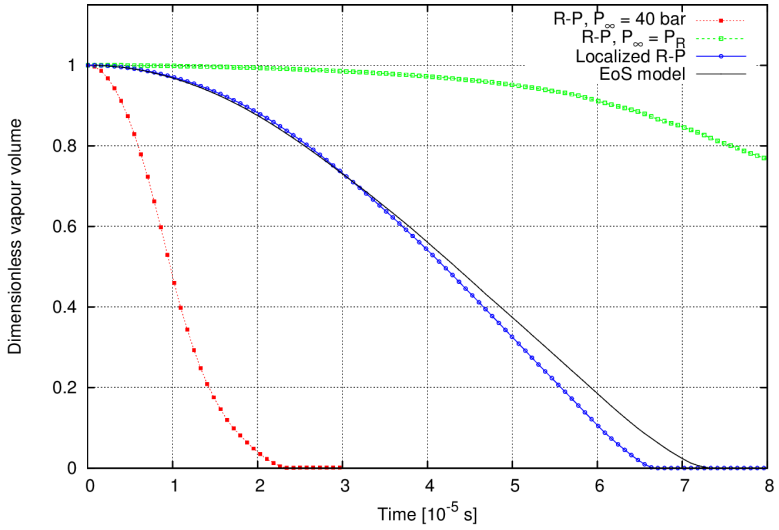

Figure 5.4: Time history of bubble cloud volume using Lagrangian model with different R–P equations.

5.3 Paper III

Analysis of the Finite Mass Transfer Models in the Numerical Simulation of Bubbly Flows

The aim of this paper is to explain the effect of empirical constants on the performance of the finite mass transfer models and to investigate some numerical issues of the model for further understanding of its performance.

As stated in Paper II, the TEM model prediction is dependent on the empirical constants of the finite mass transfer model. In the simulation of the single bubble collapse problem, with small empirical constants some numerical pulses are detected in the estimated pressure profile, especially during the last steps of bubble collapse. The numerical pulses can be avoided by using large empirical constants, however, this can suppress the peak values of the pressure profile. It can be seen in Figure 5.2 that with large empirical constants ($C_c = C_v = 10^4$), the numerical pressure peak for each time instance is lower than the corresponding theoretical value. The same issue arises when the vapour bubble is not sufficiently discritized by enough number of grid cells or the time step size is increased. To investigate the possible sources of this inconsistency in the finite mass transfer approach, in Figure 5.5, the pressure profile is predicted using this model in a different way. Here, instead of calculating the vapour fraction from the transport equation (Eq. 3.6), it is obtained from the exact analytical solution of the Rayleigh-Plesset equation. The figure shows the numerical results with two grid sizes and Δ/R is the relative cell size with respect to initial bubble radius. The other solution parameters and governing equations are the same as for the case in Figure 5.2. It is seen that in this case, the pressure profiles are predicted with high accuracy even when using a coarser grid.

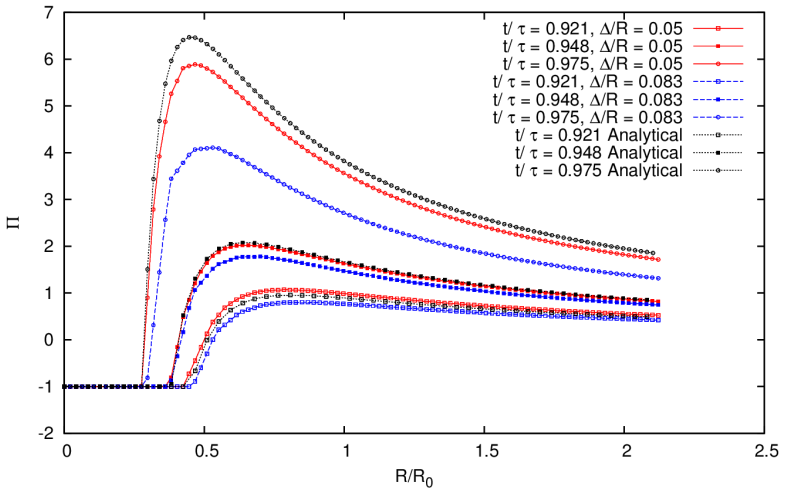

Figure 5.5: Estimated pressure profile of the finite mass transfer model with the exact solution of the bubble interface.

The issue with the model might be from the solution algorithm. In order to have a more stable solution and diagonal dominancy of the coefficient matrix, for discritization of the α transport equation, it is rewritten as [45],

$$\frac{\partial \alpha}{\partial t} + \frac{\partial (\alpha u_i)}{\partial x_i} = \frac{\dot{m}}{\rho_l} + \alpha \left(\frac{\partial u_i}{\partial x_i} - \frac{\partial u_i}{\partial x_i} \right). \tag{5.1}$$

While theoretically, the two velocity divergence terms on the right hand side should be identical, in the discretized equations one term is replaced by the continuity equation source term and the other term is calculated from the velocity field. Since the continuity equation and the volume fraction transport equation (and its corresponding source term) are not solved simultaneously for each solution iteration, these two terms are not necessarily equal and it can cause some numerical error in the solution of the volume fraction transport equation.

5.4 Paper IV

Experimental and numerical study of cavitating flow around a surface mounted semi-circular cylinder

The aim of this paper is to understand different features of the cavitating flow around a bluff body (Figure 4.1), with a special objective to find a suitable multi-scale cavitating case for validation of the hybrid solver.

Various 3D cavities around the body are investigated, from cavitation inception to super cavities. Figure 5.6 shows the average cavity pattern for different cavitation numbers. Details of the depicted cases are given in Table 4.1. In this paper, two of the test cases are also investigated numerically using the Eulerian mixture model. Based on the observed results, vortex shedding can have different patterns. While at higher cavitation numbers the vortices are shed in a cyclic

pattern, at very low cavitation numbers large fixed cavities, attached to the bluff body, are formed in the wake area. For mid-range cavitation numbers a transitional regime is seen in the shedding process. Furthermore, at very low cavitation numbers, a reverse flow is observed that moves upstream and causes the detachment of the whole cavity from the cylinder.

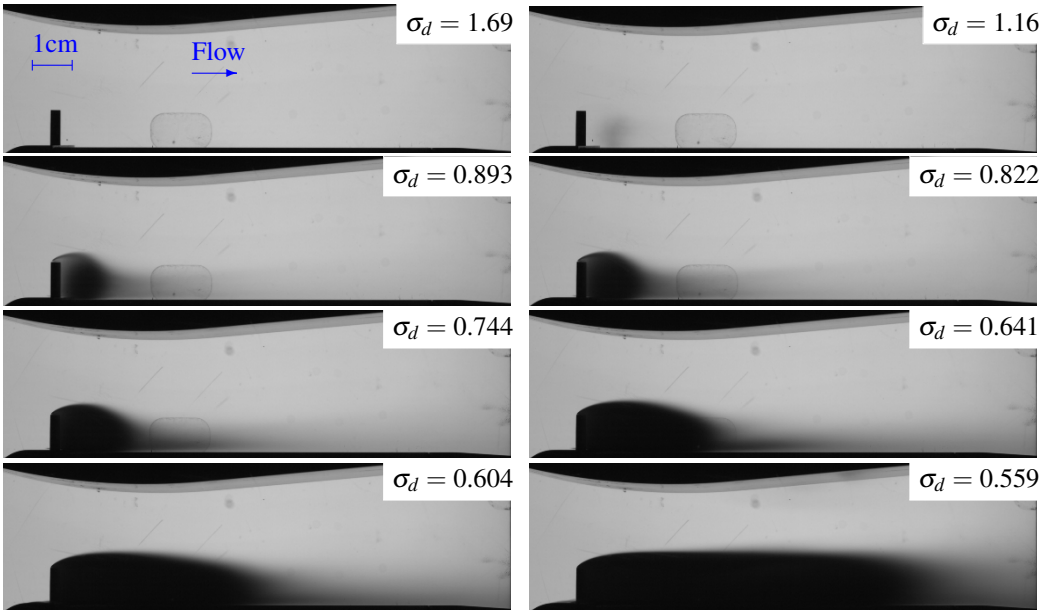

Figure 5.6: side view of the time averaged cavities for different test cases.

As the cyclic cavity pattern with $\sigma_d = 0.893$ has been chosen as a test case for validation of the hybrid model (in Paper V), here we describe more details of this case. By cyclic pattern it means that cavities are shed periodically from the cylinder wake region. Figure 5.7 shows a time series of cavity development for this case. After separation of the flow from the cylinder edges, different vortices are generated in the streamwise, spanwise and transverse directions. Here, by streamwise we mean the main flow direction, while spanwise is the direction along the cylinder span and normal to the flat plate and transverse is the other cross-stream direction normal to the spanwise direction. The low pressure vortices are firstly generated in the spanwise and transverse directions, and from their interactions with each other and the main flow, secondary streamwise vortices are created afterwards. At time T_0, a spanwise cavitating vortex, C31, is created on the cylinder surface. As this vortex detaches from the cylinder, its vapour content increases and the cavity grows ($T_0 + 5\Delta T$). Meanwhile, a second larger spanwise cavity, C32, is seen downstream of C31. While the first cavity is developing behind the cylinder, the second one is shed from the body and its vapour content is decreasing, ($T_0 + 22\Delta T$). Finally, at time $T_0 + 51\Delta T$ the second cavity is detaching in the form of a horseshoe vortex while C31 is completely developed and has a similar shape as of the second cavity in the beginning of the time series. It should be mentioned that the spanwise cavitating vortices are not always distinct from each

other, and sometimes a spanwise cavity may grow and interact with a subsequent spanwise cavity as well as other vapour structures and evolve to a larger vapour pocket. Therefore, at some instances, dense cavities with high vapour content can be seen behind the cylinder, while at another time the near-wake cavities are fully or partially transparent.

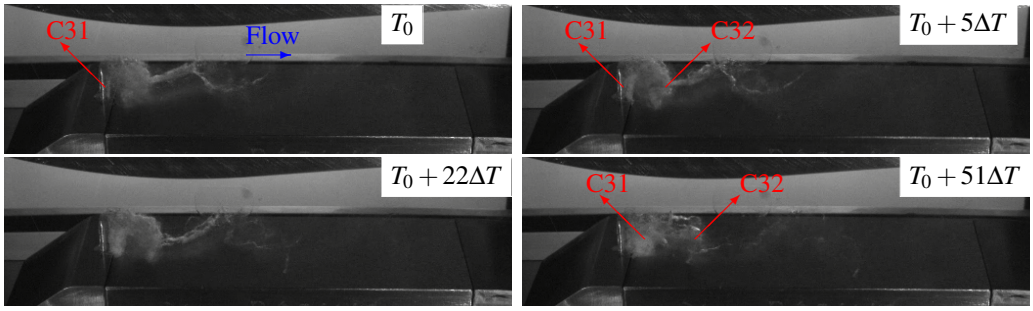

Figure 5.7: A time series of cavity structures for $\sigma_d = 0.893$; $\Delta T = 4 \times 10^{-5}$ s.

By reducing the cavitation number to $\sigma_d = 0.64$ or lower, we reach fixed cavity patterns in which a major portion of the cavity remains attached to the body and small portions shed from the trailing edge of the attached part. In Figure 5.8, two time instances of the cavity structures for such a case are shown to demonstrate some features of the flow. The dynamics and shape of the fixed cavity have considerable variations with time. Sometimes this cavity has a smooth interface with the surrounding liquid (e.g. Figure 5.8(a)), while at another time this surface can be quite disturbed (e.g. Figure 5.8 (b)). Also, sometimes the fixed cavity gets detached from the cylinder and moves downstream, while at the same time a new fixed cavity starts to develop from the body edges and a ring-shaped vortex cavity is generated in front of the cylinder base. Such phenomena are observed in Figure 5.8(b), where the dashed line shows the upstream end of a detached cavity.

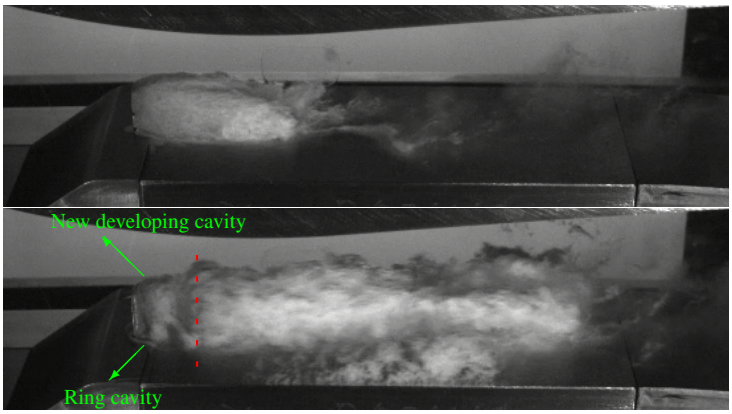

Figure 5.8: Two times instances of fixed cavity patterns: $\sigma_d = 0.641$ (top) and $\sigma_d = 0.559$ (bottom); the red dashed line locates the upstream end of the detached cavity.

5.5 PAPER V

Numerical simulation and analysis of multi-scale cavitating flows

The aim of this paper is to validate the hybrid model performance in improving the prediction of multi-scale cavitating flows and to analyse the cavitation development at different scales.

As stated earlier, in the hybrid model a cavity type (Lagrangian or Eulerian) is determined based on its relative size to the local grid cells. Therefore, the cavity type is a function of the threshold numbers, N_{EL} and N_{LE} , as well as the size of the grid cells. To investigate this influence, the flow has been simulated in four different cases, as listed in Table 5.1. In the first three cases, the simulation is performed using the main grid with 4.8 M cells, and the threshold numbers are varied. In these cases, N_{EL}, the Eulerian to Lagrangian criterion, is set to 7, 15 and 50, respectively, and the corresponding N_{LE} values are twice larger. In the last case, we simulate the flow using a coarse grid, in which the Eulerian field is less resolved as compared to the earlier cases.

Table 5.1: Simulation cases of the hybrid model

Case	N_{EL}	N_{LE}	Grid size (M cells)
N1	7	14	4.8
N2	15	30	4.8
N3	50	100	4.8
N4	15	30	1.6

In Figure 5.9, a time series of the predicted cavitation regime of case N1 is depicted. It is seen that the model can predict cavitation inception on the cylinder surface. At time T_2, the cavity HC1 starts to grow from the sharp edge of the cylinder, while a second spanwise cavity, HC2, is already developed downstream. Meanwhile we have a shedding cavity HS1 further downstream. At time $T_2+5\Delta T$, HC1 is growing while HS1 is almost a streamwise vortex. At $T_2+15\Delta T$, we can see that HS1 is still resolved as cavitating, and the cavity HC2 is shedding. Finally at $T_2+30\Delta T$, HC1 is a developed spanwise cavity similar to HC2 at time T_2. In addition, in Figure 5.9 we can see transverse cavities (as the flow separates on top of the cylinder) as well as dispersed vapour structures further downstream.

To compare the performance of the Eulerian and hybrid models, in Figure 5.10 the average cavity patterns of all numerical simulations (including the Eulerian model) are compared with the experimental result. As it is not possible to measure the liquid volume fraction from the diffuse black and white averaged image of the experiment, we plot two iso-surfaces of the numerical results. In the Figure, the black colour is the iso-surface of liquid volume fraction of 0.6, while the transparent gray colour represent the volume fraction of 0.9. Considering that we

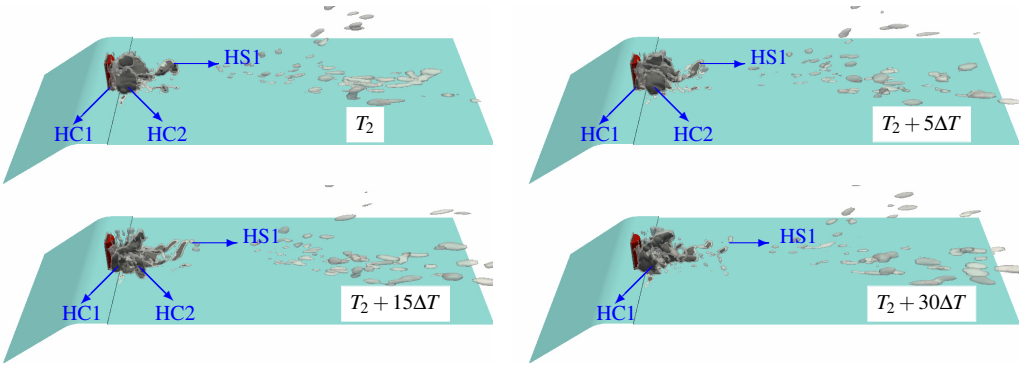

Figure 5.9: Contours of liquid volume fraction of 0.9 (light gray) and 0.5 (black) by the hybrid model, case N1.

cannot extract a quantitative volume fraction from the experiment, the numerical figures can be used for a qualitative comparison. From the averaged figure, the Eulerian model limitation in resolving the spanwise and transverse cavities in the near-wake area as well as the shedding structures is obvious. The height and length of the cavity is smaller than the real results, and even in the average cavity the liquid volume fraction is considerably lower, as no volume fraction of 0.6 is seen from the Eulerian model.

Contrarily, by considering Figures 5.9 and 5.10, it is seen that with the hybrid model, we can see considerably more cavities including transverse cavities, higher spanwise cavities starting on the body surface, shedding structures and more vapour content in the core of the averaged cavity. It is important to note that, the hybrid model causes a considerable improvement even with a lower mesh resolution (Case N4). This can significantly reduce the computational cost.

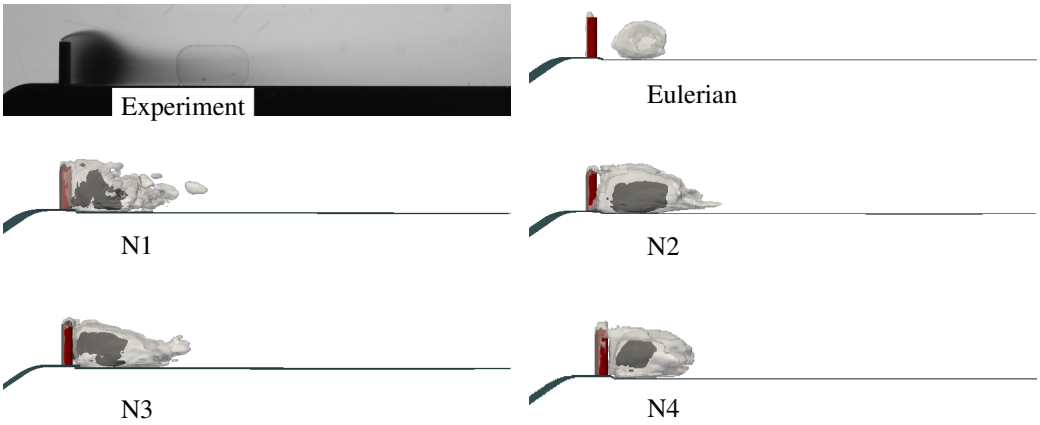

Figure 5.10: Comparison of the averaged cavity pattern of different numerical simulations with experiment. The numerical contours are liquid volume fractions of 0.9 (light gray) and 0.6 (black).

The results of cases N1-N4 share a lot of similarities and in average they predict almost similar cavity length and size. However, some minor differences are detectable in the estimated shedding cavities which can indicate some characteristics of the hybrid model. For case N1, it is seen that the shed cavities downstream are less resolved and smaller as compared to cases N2 and N3. It can be due to the lower resolution of the Eulerian cavities before their transformation to the Lagrangian bubbles in Case N1, as this case has the lowest value for N_{EL}. Therefore the transformed cavities might not be correctly initialized in the Lagrangian framework.

Also, case N3 predicts larger cavities downstream and sometimes with better resolution. However, the issue with this case is that by using large threshold numbers, sometimes we may end up with dense cavities in the Lagrangian framework which may exceed the near packing limit. In such a case the inherent assumptions for the applied models for the calculation of bubble transport and dynamics might be violated which leads to less accurate results. By comparing the cases N1-N3 it seems that, while the model has satisfactory performance in the wake area and the cavity development, the prediction of shedding cavities downstream can vary by changing the threshold numbers of the Eulerian-Lagrangian transition.

In case N4, it is seen that while the cavitation starts from the body surface and the cavities in the wake region do not have an unrealistic fast collapse, the larger cavities have less vapour content as compared to the earlier cases with a fine grid. It seems that when a Lagrangian cavity grows and is transformed to the Eulerian framework, it will not be sufficiently resolved afterwards. Case N4 shows that for obtaining sufficiently accurate results, both Eulerian and Lagrangian parts of the solver should model the corresponding structures with good accuracy.

Using the numerical results, further details of the flow field are investigated in this study. For instance, in Figure 5.11, a time series of the flow from case N2 is depicted. In the figure, we have various interacting structures including Lagrangian bubbles, Eulerian cavities and vortex structures. At this time we have a large cavity downstream and between this cavity and the cylinder there are three spanwise vortices, V1, V2 and V3. At time T_3, a large part of V1 cavitates, while inside V2 we see only Lagrangian bubbles. As the vortices move downstream, at $T_3 + 2.5\Delta T$, the cavity in the core of V1, called C1, is growing and we see that the lower part of V2 starts to cavitate, C2; by this it is meant that the Lagrangian bubbles grow so much that they are transformed to Eulerian cavities. At time $T_3 + 5\Delta T$, it is seen that the vorticity of V3 is reduced as it has more vapour content; at the same time C2 is growing. Finally, at $T_3 + 10\Delta T$, C2 has expanded so much that the vorticity of V2 is reduced such that $Q < 10^7 \mathrm{s}^{-2}$. From this time series we see that, cavitation starts at the lower part of the spanwise vortex and then it is expanded to the upper part. Also, from the figure it can be concluded that, the expansion of cavities in the wake region is not only from the growth of large-scale structures but also from the inception of other small-scale vapour pockets and their coalescence with the earlier cavities.

In addition to influencing the flow field and reducing the vorticity in the wake

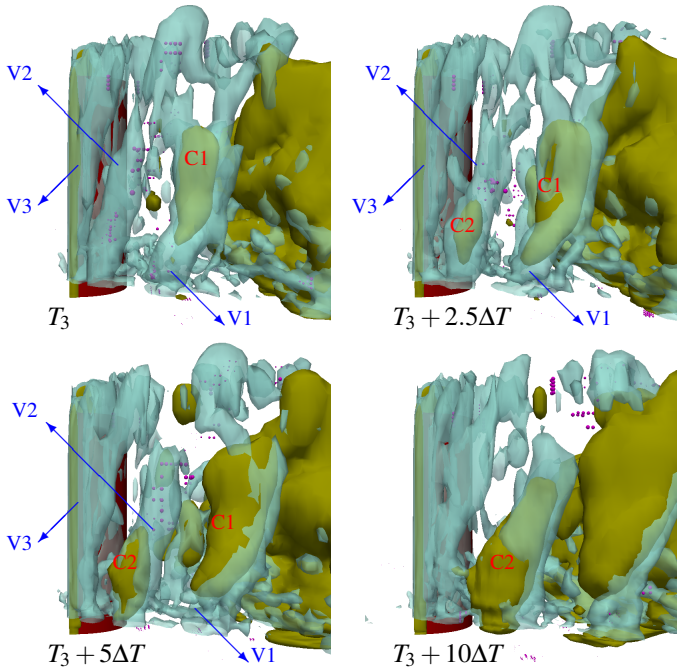

Figure 5.11: A time series of cavitation development in the spanwise vortices between a large cavity and the bluff body. The vortices are plotted with $Q \geq 10^7 s^{-2}$ (coloured in cyan); The vapour structures include Eulerian cavities (coloured in lime green) and small Lagrangian bubbles.

area, the cavities can affect the upstream flow as well. Figure 5.12 shows two different instances at which the vapour volume is rather low (left column) and high (right column). The first row of the figure shows the cavity pattern for each case. In the second row we see flow vortices via the iso-surfaces of $Q = 10^7 s^{-2}$. It is seen that with the higher vapour volume, the flow vorticity in the wake area decreases. The iso-surfaces are coloured with pressure value on a logarithmic scale. By comparing the two instances, we find that with larger cavities, the pressure in front of the cylinder is lower. This can be specifically seen in the pressures of the ring vortices just in front of the cylinder base. In the experiments, it was seen that at low cavitation numbers ($\sigma_d \leq 0.64$), a ring vortex periodically cavitates in front of the cylinder (see Figure 16 in Paper IV) and from the numerical results we now have a more clear understanding of the process. In addition, on the left and right sides of the lower wall, we see considerable variations between the two instances in pressure values and vorticity. In fact for the higher cavity volume, the pressure falls below the saturation value in some area.

Considering the difference between the pressure fields of the depicted instances in Figure 5.12, it is now possible to explain another issue with the Eulerian model in cavitation prediction on the lower wall. In the Eulerian model simulations, when the vapour volume in the wake area increases, some spurious cavities are predicted on the lower wall. The mass transfer source term in this model is

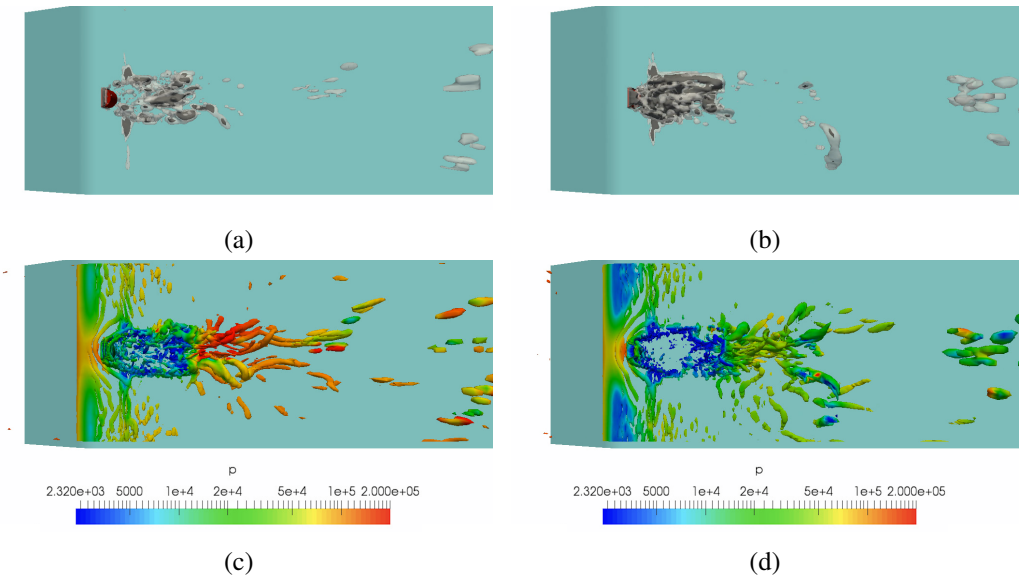

Figure 5.12: A comparison between the flow field at two instances with low and high vapour volume in the wake area. (a)-(b): Cavity structures; (c)-(d): vortical structures coloured by pressure.

mainly a function of the difference between flow pressure and saturation pressure (Eq. 3.8). As the local pressure drops below the saturation pressure on the lower wall, the liquid cavitates. By decreasing the liquid volume fraction, the mass transfer source term becomes bigger, which leads to an increase in vapour volume and a further decrease in the surrounding pressure. Therefore, after a short period of time, a sheet cavity develops on the wall, while it is not seen in the real case. We know that in reality, the size of a bubble (nucleus) does not change rapidly after a pressure drop, because of its inertia. In the current case, the pressure on the lower wall does not stay below the saturation vapour pressure and it varies over time. Furthermore, the bubble surface tension is another parameter which has an opposite effect on bubble growth, especially at small scales. These two parameters are taken into account in the Rayleigh-Plesset equation, via the first and the last terms (Eq. 3.15 in Chapter 3), and therefore the Lagrangian bubbles do not have a fast growth. As a result, in hybrid model simulations, such unrealistic cavities are avoided on the lower wall.

6

Conclusions

In this study, a hybrid mixture-bubble model was developed to calculate cavitating flows with an extensive range of length scales from large cavities to sub-grid micro-bubbles.

To understand the capabilities and limitations of different commonly used cavitation models and to find the potential area of improvements in the hybrid model, at first three different cavitation models were compared in the simulation of two benchmark test cases (Papers II and III). The models were well established equilibrium and TEM models as well as a Lagrangian bubble model that was developed in the current study. From this comparison we conclude that Eulerian models estimate a diffusive liquid-vapour interface and to have a more precise representation they need finer grids. The interface diffusivity can have considerable effect in the estimation of local pressure on the interface and the shape of cavity structure, especially in the last stages of the collapse. On the other hand, the Lagrangian model can give satisfactory results with larger time steps and coarser grids as compared to the Eulerian approaches.

Furthermore, Some numerical pulses are detected in the estimated pressure profiles of the Eulerian models for the single bubble collapse problem, and this can be significant in collapse pressure calculation for special situations. From the comparison of the TEM and Lagrangian models, it is concluded that when the sharp bubble interface is estimated precisely, these numerical issues are resolved. In summary, using a Lagrangian bubble model for the small-scale cavity structures can reduce the computational cost as larger time steps and grid size can be used, and at the same time improve the collapse pressure estimation around each single bubble. In the Lagrangian bubble model, a new form of the well-known R-P equation is developed, in which the bubble size variation is calculated based on the local pressure value around the bubble. In the bubble cluster test case (Paper II), the flow field around each bubble was unsymmetric and the correct estimation of the local pressure plays a more important role. It was shown in this case that using

the local form of the R-P equation improves the model behaviour significantly as compared to other forms of the equation used in the earlier hybrid/Lagrangian models.

After understanding the characteristics of the models, the hybrid model was implemented in OpenFOAM by coupling the TEM mixture model with the Lagrangian bubble model. For the Eulerian cavities an incompressible flow and a TEM model was considered, motivated by the lower computational cost for large-scale applications, however the coupling algorithm can be used for compressible models to take into account the relevant flow effects in other applications. It was shown that using the initial algorithm (which in basic principles follows the earlier available models) leads to spurious numerical pressure pulses, as well as spurious vapour generation and insufficient consideration of bubble contribution in the mixture behaviour.

Therefore, a solution to these issues was presented by reformulating the coupling between the bubbles and the Eulerian governing equations to more accurately include the effects of bubbles on the Eulerian flow, as well as improving the Eulerian-Lagrangian transition algorithm. This amounts to considering the total vapour in the flow, and not only the Eulerian mixture vapour fraction. Also, the generation of Eulerian cavities in the bubbly cells was avoided by revising the source term of the Eulerian vapour transport equation. In addition, during the Eulerian-Lagrangian transition process, several discrete bubbles are inserted to achieve a better representation of the spatial distribution of the Eulerian mixture during the transition. Finally, the overall improvements were verified through a qualitative simulation of the 2D cavitating flow around a hydrofoil (Paper I).

In the third part of this study, a set of experimental tests for cavitating flow around a surface mounted semi-circular cylinder was performed. In addition to finding a real 3D case from the test series for verification and validation of the solver, in this part the cavitating flow was investigated in detail to have a comprehensive understanding of the flow physics. It was found that for the current sharp edge bluff body, cavitation inception occurs along the streamwise and spanwise vortices. Contrary to earlier findings for triangular bluff bodies (e.g. [46]), the spanwise vortices are more cavitating than the secondary streamwise vortices for the current set-up.

By decreasing the cavitation number, other types of vortices, such as transverse vortices at the top edge, as well as horseshoe vortices in the wake area may cavitate. As compared to earlier studies, the current set up can generate different 3D structures as the fluid passes over the top side and sharp edges of the body. Due to the interaction between primary (spanwise and transverse) vortices as well as the high velocity gradients, secondary weaker vortices are generated in the wake area. Such structures may get a horseshoe shape or turn into a streamwise vortex.

Furthermore, in the experimental series it is observed that, while at higher cavitation numbers cavitating vortices are shed in a cyclic pattern in the wake area, for lower cavitation numbers, a large vapour structure is attached to the bluff body. A deeper investigation reveals that the axial velocity component inside this

fixed cavity is negative, showing a reverse flow in the super cavity. Also, an upstream moving disturbance jet appears in the fixed cavity which accelerates the reverse flow towards the cylinder. This disturbance affects the cavity dynamics significantly, causing its detachment from the cylinder and perturbing the liquid-vapour interface.

Another important findings in this part, which was further investigated in a later numerical analysis with the hybrid model, is the vapour structures effect on the flow dynamics and vorticities. For the cyclic shedding pattern, at the time instances that the vapour fraction in the wake area is larger, the flow vorticity is smaller as compared to other instances with lower vapour content. Also, for the fixed cavity pattern, the vapour structures significantly modify the vorticity and shape of the vortical structures, as well as their shedding pattern in the wake area. The comparison between the single-phase flow and cavitating flow simulations show that at lower cavitation numbers with fixed cavity pattern, the drag force on the cylinder is reduced and the temporal plot of the drag force has local minimum at the instances when the disturbance jet hits the bluff body.

In the last part, a multi-scale cavitation problem was investigated using the new hybrid model. This test case is a cyclic cavitating flow from the experimental series. To make the model applicable to a complex 3D problem, it was considerably improved further in this part. The improvements include the new introduced submodels in the Lagrangian framework to consider bubble-bubble interactions and break-up, more accurate estimation of the void handling scheme, correcting the bubble-wall boundary condition, and introducing bubble parcels to reduce the computational costs. Furthermore, in the Eulerian-Lagrangian transition algorithm, the properties of the new injected bubbles (specially $\dot{R}$ and $\ddot{R}$) are initialized based on the dynamics of the old Eulerian structures, in contrary to the earlier hybrid models, in which a bubble is assumed to be in equilibrium condition with a zero initial collapse rate. Therefore, considering the previous and new corrections in the transition algorithm, it is more compatible with the flow physics, as compared to the earlier hybrid models. Also, the cavities' mass, momentum and kinetic energy are conserved during the transition.

The obtained results show considerable improvements in numerical simulation of multi-scale cavitation, as compared to the commonly used Eulerian mixture model. The improvements include capturing the cavitation inception on the surface of the bluff body, avoiding spurious cavities on the lower wall and modelling the sub-grid vapour structures not only in the wake area around the larger cavities but also the shedding vortices and disperse clouds downstream. The results show that the improved performance can be achieved even with noticeably lower mesh resolution which can reduce the computational cost. The model comparison clarifies further the numerical issues with the Eulerian models. In addition to the well-known higher dependency on the grid resolution, the common Eulerian models do not give an appropriate estimation of the cavity inertia, and as cavitation is modelled only based on the pressure variations, the cavity dynamics is highly dependant on temporal variations of the pressure. As a consequence,

fast temporal pressure variation causes spurious cavitation on the lower wall and higher condensation rate in the wake area.

The numerical results also show that the cyclic cavity development and shedding in the wake area is a very unsteady process with various interactions between the large and small-scale cavities as well as the continuous flow. The larger cavities are not only developed from growing of a spanwise cavitating vortex, but also the vaporization of other vortices and the smaller vapour structures at subgrid scales and the coalescence of these structures. Such vaporization and the coalescence probability are dependent on the flow vorticity and pressure fields in the near-wake area which are, in turn, influenced by the downstream cavities. With lower vapour volume only a fraction of spanwise vortices cavitate from their lower part and after travelling a minimum distance from the body. With increasing vapour volume in the wake area, the cavitation starts from the bluff body surface with more frequent vaporization of spanwise and transverse vortices. At larger volumes, the generated cavity can considerably influence the flow upstream of the cylinder which explains the periodic cavities on the lower wall and ring shape vortices in front of the body which are observed for lower cavitation numbers (see Paper IV).

Finally, a comparison between different cases of the hybrid simulation further clarifies the model characteristics. From this comparison, we conclude that for satisfactory simulations, both Eulerian and Lagrangian parts should model the corresponding structures with sufficient accuracy.

7

Future work

In this study we used a common Eulerian model and the improvements were more focused on the Lagrangian modelling and the transition algorithm. As stated, the common Eulerian models do not give an appropriate estimation of the cavity inertia, and the cavity dynamics is highly dependant on temporal variations of the pressure. Therefore, fast temporal pressure variation causes spurious vapour generation or higher condensation rates. To increase the model accuracy, the Eulerian model can be improved as well. One suggestion in this regard is to include the flow history effect or pressure variation rate in the mass transfer modelling. Another suggestion is to implement the cavity inertia effect (e.g. $\dot{V}$ or $\ddot{V}$) in the condensation/vaporization rates of finite mass transfer models.

In addition, from the comparison of different hybrid model simulations, it is found that the prediction of shedding cavities at downstream can vary by changing the threshold numbers (N_{EL} and N_{LE}) of the Eulerian-Lagrangian transition. For a more numerically robust transition between the Eulerian and Lagrangian frameworks, a more elaborate transition criterion can be defined that is based more on the cavity dynamics and considers non-uniformity of domain discretization. Furthermore, the cavitation inception can be based on free nuclei in the liquid and on solid walls. Although the inception is well represented in the current problem, introducing nuclei can make the inception process more independent from the Eulerian simulation and adds the possibility to consider liquid quality.

Further improvement of the model can be achieved by quantitative validation of the solver and the calibration of the various parameters in the developed submodels. The experimental test case of the current study included various scales of vapour structures and different phenomena from inception, cavity development, shedding and collapse of vapour structures, which also helped to understand some limitations of the Eulerian model as well. However, due to the limitations of the measurement techniques, it lacks enough measured data for quantitative validation of the Lagrangian submodels and to calibrate the model constants. For this purpose special experimental tests or more accurate Direct Numerical Simulations

are needed. For instance, there are detailed simulations of special cases of bubble clusters in literature (e.g. [18] and [38]), in which bubble collisions are ignored or only bubble coalescence is taken into account. However, more advanced cases are needed to validate the Lagrangian submodels. Such cases can be a bubble cluster in a turbulent flow where bubble/parcel collision in more complex situations and cavitating bubble breakup are investigated in detail. Furthermore, it will be beneficial to have more comprehensive cases (such as the applied test case but) with flow quantities that are measured in detail and a continuum flow field that can be modelled with more certainty. When the Reynolds number is very high and the flow has different complex structures (as for the current test case), it is difficult to find if the numerical issues are due to the insufficient continuum flow calculations or mass transfer modelling, for example.

Finally, the model can be improved to be applied in cavitation noise prediction and erosion risk assessment as well. It may be done by incorporation of the radiated acoustic pressure wave due to bubble collapse and rebound (similar to [47] and [48]) or implementing the liquid compressibility effect in the solver. From the bubble cluster test case (Paper II), it is seen that considering the fluid compressibility may cause difference in cavitation modelling in general. It should be reminded that both the applied homogeneous mixture model as well as the developed Rayleigh-Plesset equation are based on the hypothesis that thermodynamic and compressibility effects are negligible for the considered applications. When the thermal variations are considerable or we are modelling the cavity dynamics at micro scales or the emitted pressure waves, these effects should be taken into account. In paper II, the results with the three models show that considering the (pure phase) compressibility is effective in the estimation of the flow pressure and to have a reliable study of the cavity collapse pressure it is necessary to consider this parameter. However, from the comparison of the cavity structures of the compressible (EoS) and incompressible (TEM and Lagrangian) simulations, it is seen that even by ignoring the fluid compressibility, the collapse rate and vapour distribution can be predicted with reasonable accuracy. From this point, it can be concluded that the hybrid mixture-bubble model is capable of representing the cavity dynamics even when ignoring the pure phase compressibility. However, to calculate the erosion risk assessments, where the collapse pressure pulses are taken into account, either the liquid compressibility effect should be considered in the model, or another erosion indicator based on the mixture and bubble dynamics should be implemented in the solver.

REFERENCES

[1] J-P. Franc and J-M. Michel. *Fundamentals of cavitation*, volume 76. Springer Science & Business Media, 2006.

[2] E. Vlaisavljevich, A. Maxwell, L. Mancia, E. Johnsen, C. Cain, and Z. Xu. Visualizing the histotripsy process: Bubble cloud–cancer cell interactions in a tissue-mimicking environment. *Ultrasound in medicine & biology*, 42(10):2466–2477, 2016.

[3] S. Ibsen, C. E. Schutt, and S. Esener. Microbubble-mediated ultrasound therapy: a review of its potential in cancer treatment. *Drug design, development and therapy*, 7:375, 2013.

[4] K. Maeda, T. Colonius, W. Kreider, A. Maxwell, and M. Bailey. Modeling and experimental analysis of acoustic cavitation bubble clouds for burst-wave lithotripsy. *The Journal of the Acoustical Society of America*, 140(4):3307–3307, 2016.

[5] H. Mulvana, R. J. Browning, Y. Luan, N. de Jong, M-X. Tang, R. J. Eckersley, and E. Stride. Characterization of contrast agent microbubbles for ultrasound imaging and therapy research. *IEEE transactions on ultrasonics, ferroelectrics, and frequency control*, 64(1):232–251, 2016.

[6] E-J. Foeth and T. van Terwisga. The structure of unsteady cavitation, part I: Observation of an attached cavity on a three-dimensional hydrofoil. In *Proceedings of 6th International Symposium on Cavitation, Wageningen, The Netherlands*, 2006.

[7] A. Asnaghi, U. Svennberg, and R. E. Bensow. Numerical and experimental analysis of cavitation inception behaviour for high-skewed low-noise propellers. *Applied Ocean Research*, 79:197–214, 2018.

[8] B. Budich, S.J. Schmidt, and N. A. Adams. Numerical simulation and analysis of condensation shocks in cavitating flow. *Journal of Fluid Mechanics*, 838:759–813, 2018.

[9] A. Gnanaskandan and K. Mahesh. Numerical investigation of near-wake characteristics of cavitating flow over a circular cylinder. *Journal of Fluid Mechanics*, 790:453–491, 2016.

[10] G. H. Schnerr, I. H. Sezal, and S. J. Schmidt. Numerical investigation of three-dimensional cloud cavitation with special emphasis on collapse induced shock dynamics. *Physics of Fluids*, 20(4):040703, 2008.

[11] A. H. Koop. *Numerical simulation of unsteady three-dimensional sheet cavitation*. PhD thesis, University of Twente, 2008.

[12] T. Barberon and P. Helluy. Finite volume simulation of cavitating flows. *Computers & fluids*, 34(7):832–858, 2005.

[13] H. Meng and V. Yang. A unified treatment of general fluid thermodynamics and its application to a preconditioning scheme. *Journal of Computational Physics*, 189(1):277–304, 2003.

[14] R. Saurel, P. Cocchi, and P. B. Butler. Numerical study of cavitation in the wake of a hypervelocity underwater projectile. *Journal of Propulsion and power*, 15(4):513–522, 1999.

[15] G. H. Schnerr and J. Sauer. Physical and numerical modeling of unsteady cavitation dynamics. In *Fourth international conference on multiphase flow, New Orleans, USA*, volume 1, 2001.

[16] V. H. Arakeri. Viscous effects on the position of cavitation separation from smooth bodies. *Journal of Fluid Mechanics*, 68(04):779–799, 1975.

[17] A. Asnaghi, A. Feymark, and R.E. Bensow. Numerical investigation of the impact of computational resolution on shedding cavity structures. *International Journal of Multiphase Flow*, 107:33–50, 2018.

[18] D. Fuster and T. Colonius. Modelling bubble clusters in compressible liquids. *Journal of Fluid Mechanics*, 688:352–389, 2011.

[19] E. Giannadakis, M. Gavaises, and C. Arcoumanis. Modelling of cavitation in diesel injector nozzles. *Journal of Fluid Mechanics*, 616:153–193, 2008.

[20] E. Shams, J. Finn, and S.V. Apte. A numerical scheme for Euler–Lagrange simulation of bubbly flows in complex systems. *International Journal for Numerical Methods in Fluids*, 67(12):1865–1898, 2011.

[21] D. Kim, M. Herrmann, and P. Moin. The breakup of a round liquid jet by a coaxial flow of gas using the refined level set grid method. In *APS Division of Fluid Dynamics Meeting Abstracts*, 2006.

[22] M. Herrmann. A parallel Eulerian interface tracking/Lagrangian point particle multi-scale coupling procedure. *Journal of Computational Physics*, 229(3):745–759, 2010.

[23] G. Tomar, D. Fuster, S. Zaleski, and S. Popinet. Multiscale simulations of primary atomization. *Computers & Fluids*, 39(10):1864–1874, 2010.

[24] H. Ström, S. Sasic, O. Holm-Christensen, and L. J. Shah. Atomizing industrial gas-liquid flows–development of an efficient hybrid VOF-LPT numerical framework. *International Journal of Heat and Fluid Flow*, 62:104–113, 2016.

[25] C-T. Hsiao, J. Ma, and G. L. Chahine. Multiscale tow-phase flow modeling of sheet and cloud cavitation. *International Journal of Multiphase Flow*, 90:102–117, 2017.

[26] A. Vallier. *Simulations of cavitation-from the large vapour structures to the small bubble dynamics*. PhD thesis, Lund University, ISBN 978-91-473-517-8, 2013.

[27] A. K. Lidtke. *Predicting radiated noise of marine propellers using acoustic analogies and hybrid Eulerian-Lagrangian cavitation models*. PhD thesis, University of Southampton, 2017.

[28] A. Peters and O. el Moctar. Numerical assessment of cavitation-induced erosion using a multi-scale Euler–Lagrange method. *Journal of Fluid Mechanics*, 894, 2020.

[29] OpenFoam. *The Open Source CFD Toolbox openfoam foundation. http://www.openfoam.com*, Accessed: 2018-01-15, 2018.

[30] H. G. Weller, G. Tabor, H. Jasak, and C. Fureby. A tensorial approach to computational continuum mechanics using object-oriented techniques. *Computers in physics*, 12(6):620–631, 1998.

[31] H. Jasak. *Error Analysis and Estimation for the finite volume method with applications to fluid flows*. PhD thesis, Department of Mechanical Engineering, Imperial College of Science, 1996.

[32] H. Rusche. *Computational fluid dynamics of dispersed two-phase flows at high phase fractions*. PhD thesis, Imperial College London (University of London), 2003.

[33] R. E. Bensow and G. Bark. Implicit LES predictions of the cavitating flow on a propeller. *Journal of fluids engineering*, 132(4):041302, 2010.

[34] D. Drikakis, M. Hahn, A. Mosedale, and B. Thornber. Large eddy simulation using high-resolution and high-order methods. *Philosophical Transactions of the Royal Society A: Mathematical, Physical and Engineering Sciences*, 367(1899):2985–2997, 2009.

[35] S. Schenke and T.J.C. van Terwisga. Simulating compressibility in cavitating flows with an incompressible mass transfer flow solver. In *Proc. of the Fifth International Symposium on Marine Propulsors, smp'17, Espoo, Finland*, volume 1, pages 71–79, 2017.

[36] M. Breuer and M. Alletto. Efficient simulation of particle-laden turbulent flows with high mass loadings using LES. *International journal of heat and fluid flow*, 35:2–12, 2012.

[37] A.M. Kamp, A.K. Chesters, C. Colin, and J. Fabre. Bubble coalescence in turbulent flows: a mechanistic model for turbulence-induced coalescence applied to microgravity bubbly pipe flow. *International Journal of Multiphase Flow*, 27(8):1363–1396, 2001.

[38] Y. A. Ilinskii, M. F. Hamilton, E.A. Zabolotskaya, and G.D. Meegan. Influence of compressibility on bubble interaction. In *AIP Conference Proceedings*, volume 838, pages 303–310. American Institute of Physics, 2006.

[39] Y.M. Lau, W. Bai, N.G. Deen, and J.A.M. Kuipers. Numerical study of bubble break-up in bubbly flows using a deterministic Euler–Lagrange framework. *Chemical Engineering Science*, 108:9–22, 2014.

[40] F. Hoppe and M. Breuer. A deterministic breakup model for Euler–Lagrange simulations of turbulent microbubble-laden flows. *International Journal of Multiphase Flow*, 123:103119, 2020.

[41] S. V. Patankar and D. B. Spalding. A calculation procedure for heat, mass and momentum transfer in three-dimensional parabolic flows. In *Numerical Prediction of Flow, Heat Transfer, Turbulence and Combustion*, pages 54–73. Elsevier, 1983.

[42] I. E. Barton. Comparison of SIMPLE-and PISO-type algorithms for transient flows. *International Journal for numerical methods in fluids*, 26(4):459–483, 1998.

[43] S.J. Schmidt, M. Mihatsch, M. Thalhamer, and N.A. Adams. Assessment of the prediction capability of a thermodynamic cavitation model for the collapse characteristics of a vapor-bubble cloud. In *WIMRC 3rd International Cavitation Forum*. University of Warwick UK, 2011.

[44] S. J. Schmidt, M. S. Mihatsch, M. Thalhamer, and N. A. Adams. Assessment of erosion sensitive areas via compressible simulation of unsteady cavitating flows. In *Advanced experimental and numerical techniques for cavitation erosion prediction*, pages 329–344. Springer, 2014.

[45] A. Asnaghi. *Developing computational methods for detailed assessment of cavitation on marine propellers*. PhD thesis, Department of Shipping and Marine Technology, Chalmers University of Technology, 2015.

[46] H. Ganesh, L. Deijlen, A. Bhatt, J. Wu, and S. L. Ceccio. Cavitation dynamics in wakes of bluff bodies. In *32nd Symposium on Naval Hydrodynamics*. Hamburg, Germany 5-10 August 2018, 2018.

[47] C. Eskilsson and R. E. Bensow. Estimation of cavitation erosion intensity using CFD: numerical comparison of three different methods. *sign (p- pv)*, 3:2, 2015.

[48] N. Ochiai, Y. Iga, M. Nohmi, and T. Ikohagi. Numerical prediction of cavitation erosion intensity in cavitating flows around a Clark Y 11.7% hydrofoil. *Journal of Fluid Science and Technology*, 5(3):416–431, 2010.

APPENDIX A

Appended Papers I-V